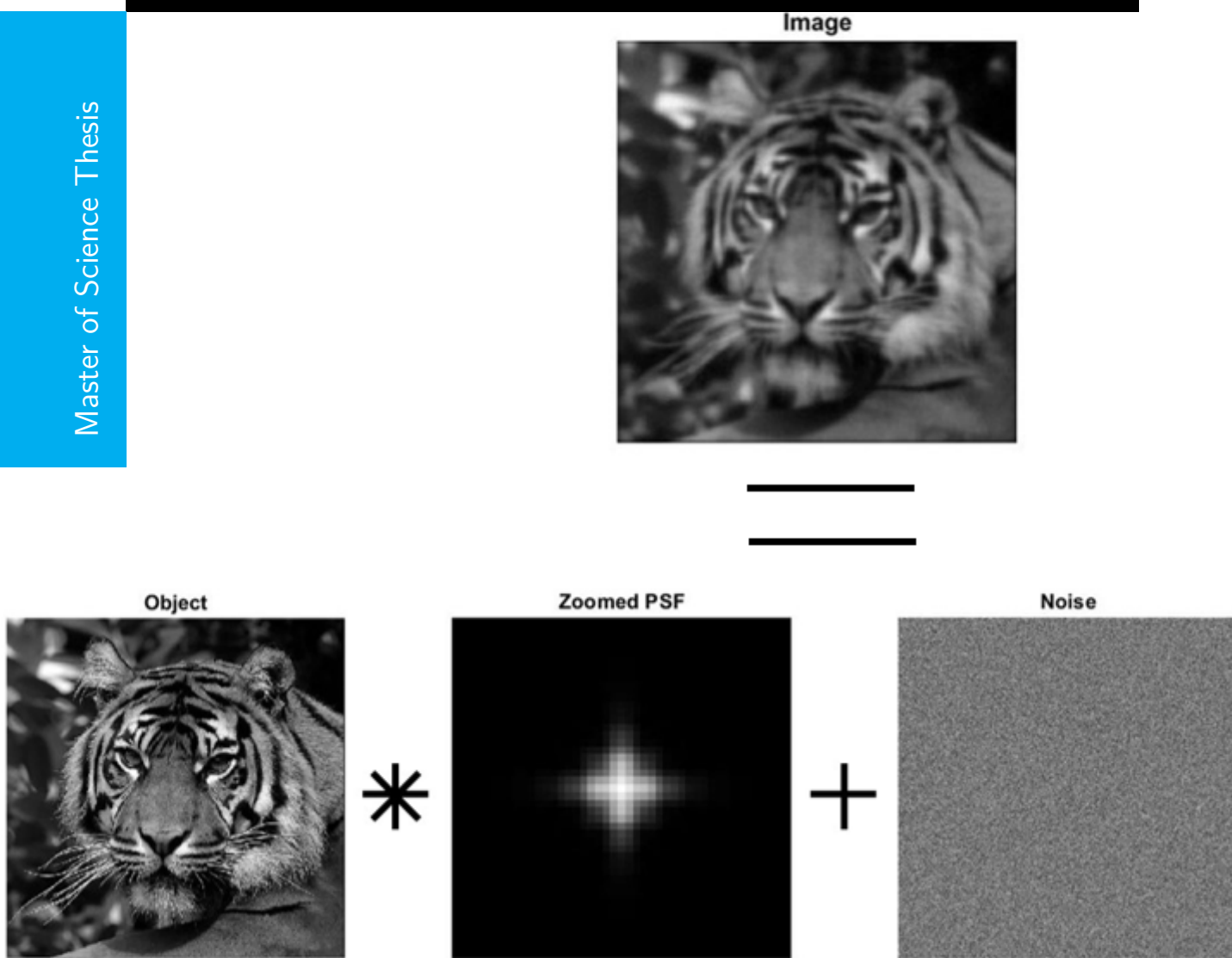


Phase Diversity for Blind Multi-Frame Deconvolution

Dominique Vrijburg

Master of Science Thesis



Phase Diversity for Blind Multi-Frame Deconvolution

MASTER OF SCIENCE THESIS

For the degree of Master of Science in Systems and Control at Delft
University of Technology

Dominique Vrijburg

June 29, 2021

Faculty of Mechanical, Maritime and Materials Engineering (3mE) · Delft University of
Technology



Copyright © Delft Center for Systems and Control (DCSC)
All rights reserved.



Abstract

When objects are imaged, often aberrations slip into the captured images. Many techniques exist to remove part of those aberrations using hardware, software or a combination of those. This research will focus on Phase Diversity for Blind Multi-Frame Deconvolution. In Blind Multi-Frame Deconvolution both the object and the aberrations are estimated from multiple images of the same object. Previous research has shown, Phase Diversity can be used to improve the quality of the reconstructed object in combination with Blind Multi-Frame Deconvolution. Using Defocus Phase Diversity is currently mainly used in literature.

In this research new Phase Diversity methods are proposed. When there is no knowledge on the object or aberrations, Phase Diversities are proposed to improve the object reconstruction compared to Defocus Phase Diversity.

We also propose a new method to optimize the Phase Diversity for the $N + 1^{th}$ image, when already N images have been taken. This method first determines the low values in the frequency spectra of the images. Next it estimates a Phase Diversity that results in a Modulation Transfer Function to enhance those frequencies. This method leads to an improved restoration quality in terms of Structural Similarity and Peak Signal to Noise Ratio when there is Gaussian noise or Poisson noise with a higher Signal to Noise Ratio. Recommendations are done to improve the method for lower Signal to Noise Ratios.

Table of Contents

Acknowledgements	ix
1 Introduction	1
2 Image formation.	5
2-1 Image of a point source	5
2-1-1 Pupil function	5
2-1-2 Distorted wavefront	6
2-1-3 Amount of wavefront error	7
2-1-4 Point Spread Function	7
2-2 Image of an extended object	7
3 Deconvolution methods in imaging	9
3-1 Deconvolution with a known Point Spread Function (PSF)	9
3-1-1 Inverse Filtering	9
3-1-2 Wiener Filter	10
3-1-3 Tikhonov Miller filter	10
3-1-4 Comparison of the Inverse, Modified Wiener and Tikhonov Miller filter	11
3-2 Estimating the wavefront from the PSF	11
3-3 Blind multi-frame deconvolution for extended objects using Phase Diversity	11
3-3-1 Blind Multi-frame Deconvolution using knowledge on Phase Diversity	13
3-3-2 Tangential Iterative Projection algorithm	13
3-4 Quality of the restored object	15
3-4-1 Mean Squared Error (MSE) and Peak Signal to Noise Ratio (PSNR)	15
3-4-2 Structural Similarity (SSIM)	15
3-4-3 Sharpness	16
3-4-4 Comparison of the metrics	16

4	Diversity Methods in Literature.	19
4-1	Purpose of Diversity	19
4-2	Examples of Diversity in Literature.	20
4-2-1	Amplitude Diversity.	20
4-2-2	Phase Diversity	21
4-2-3	Wavelength diversity	23
4-3	Determining diversity based on aberrations	24
4-3-1	Optimizing the channel capacity	24
4-3-2	Optimizing Phase Diversity for a neural network	24
4-4	Conclusions	25
5	Predefined Phase Diversity for Blind Deconvolution	27
5-1	New Phase Diversity Shapes based on Shapes in Literature	27
5-1-1	Rotating phase Phase Diversity	27
5-1-2	Rotating half phase Phase Diversity	28
5-1-3	Spiral Phase Diversity with TIP	29
5-2	Optimization based phase diversities	29
5-2-1	Optimizing Modulation Transfer Functions in terms of PSNR	30
5-2-2	Optimizing Modulation Transfer Functions in terms of SSIM	31
5-2-3	Optimizing Modulation Transfer Functions in terms of Miyamura's metric.	31
5-3	Simulations	32
5-4	Results of the simulations	33
5-4-1	Rotating phase and rotating half phase	34
5-4-2	Spiral Phase Diversity	35
5-4-3	Optimized Phase Diversities	36
5-4-4	Conclusions on the proposed predefined Phase diversities.	37
6	Phase Diversity Dependent on Previous Images	43
6-1	Finding the decreased frequencies.	43
6-2	Designing the Phase Diversity	44
6-3	Results of method for defining the Phase Diversity for the N+1th image	46
6-3-1	Gaussian noise	46
6-3-2	Poisson noise	47
6-3-3	Optimized Phase Diversities	48
6-3-4	Conclusion	49
7	Conclusions and Recommendations	55
A	Zernike Polynomials at Nolls order	57
	Bibliography	59
	Glossary	63
	List of Acronyms	63

List of Figures

2-1	Example of a) a Lower order, b) Kolmogorov and c) sparse aberrated wavefront.	6
2-2	Image formation with isoplanatic aberrations	8
3-1	An example of object restoration with different deconvolution methods.	12
3-2	A visualisation of the steps in the Tangential Iterative Projection (TIP) algorithm [1].	14
3-3	Different deteriorated images to compare quality metrics.	18
4-1	Amplitude diversity mask with the rotating disk and its corresponding PSF	20
4-2	The spiral phase mask from Sharma <i>et al</i>	22
4-3	An approximation of the optimally informative saddle point phase pattern from Shechtman with in and out of focus PSFs.	23
4-4	The cubic phase mask from Dowski and its corresponding PSF	23
5-1	Rotating phase Phase Diversity	28
5-2	PSFs of the rotating amplitude disk from literature and the proposed rotating phase Phase Diversity (PD).	28
5-3	Rotating half phase Phase Diversity	29
5-4	Phase of the spiral phase mask applied to four images.	29
5-5	Phase diversity obtained by optimizing the PSNR	30
5-6	Phase diversity obtained by optimizing the SSIM	31
5-7	Phase diversity obtained by optimizing Miyamuras metric	32
5-8	Objects used in simulations and the corresponding Fourier transforms	34
5-9	Quality of object reconstruction using rotating phase PD with sparse wavefront with P-V error= $4/7 \pi$ and Poisson noise.	35
5-10	Quality object reconstructions for the rotating phase PD and rotating half phase PD, for lower order wavefronts with Gaussian noise $\sigma = 0.005$	36

5-11	Quality object reconstructions for the rotating phase PD and rotating half phase PD, for Kolmogorov phase screens with Gaussian noise $\sigma = 0.005$	37
5-12	Quality of object reconstruction using rotating phase PD with lower order wavefront with RMS=1 and Poisson noise.	38
5-13	Visual example of object reconstruction for proposed diversities when Poisson noise is present in the image	39
5-14	Quality of object reconstruction using rotating phase PD and spiral PD with lower order wavefront with RMS=1 and Poisson noise.	40
5-15	Quality of object reconstructions using the MTF optimized phase diversities, Kolmogorov wavefronts and Gaussian noise with $\sigma = 0.01$ are used.	41
5-16	Quality of object reconstructions using the MTF optimized phase diversities, Poisson noise and lower order wavefronts with a RMS wavefront error is 1 are used.	41
6-1	On the left the Siemens star, in the middle a variation where the highest 50% of the frequencies have been removed and on the right a version where the lowest 2% of the frequencies have been removed.	44
6-2	An visual example of the method used to determine the PD for the N+1th image.	45
6-3	Quality of object reconstruction using the proposed PD method with Lower order wavefront and gaussian noise $\sigma = 0.005$	47
6-4	Quality of object reconstruction using the proposed PD method with Kolmogorov wavefront and gaussian noise $\sigma = 0.005$	48
6-5	This example shows object 1: the tiger, and the restorations of it for using no PD, Defocus PD and the optimized PD. Below the restorations the PSNR and SSIM are given. Here a lower order wavefront with a Root Mean Square (RMS) of 0.75 was used as the aberration and the Gaussian noise has a standard deviation of $\sigma = 0.005$	49
6-6	Quality of object reconstruction using the proposed PD method with lower order wavefront and Poisson noise $\sigma = 0.005$	50
6-7	This example shows object 1: the tiger, one image without diversity applied and the restorations of it for using no PD, Defocus PD and the optimized PD. Below the restorations the PSNR and SSIM are given. Here a lower order wavefront with a RMS of 1 was used as the aberration and the Poisson noise has a SNR of 28 dB.	51
6-8	This example shows object 1: the tiger, one image without diversity applied and the restorations of it for using no PD, Defocus PD and the optimized PD. Below the restorations the PSNR and SSIM are given. Here the same lower order wavefront with a RMS of 1 was used as in Figure 6-7, this time Poisson noise has a SNR of 52 dB.	51
6-9	A visual example of a created weighting mask W , the corresponding optimized Modulation Transfer Function (MTF) and PD and the object reconstruction with and without this PD.	52
6-10	The amplitude of the Zernike polynomials in the optimized PDs for all parameters in Table 5-1. It has been split up in lower order and Kolmogorov wavefronts and in Gaussian and Poisson noise.	53
A-1	Zernike polynomials at Nolls order	58

List of Tables

3-1	Comparing the quality metrics Peak Signal to Noise Ratio, SSIM and Sharpness .	16
5-1	Parameters used in simulations, the objects can be found in Figure 5-8.	33

Acknowledgements

This report is part of my Master of Science graduation thesis for the Master Systems and Control. When I started my masters I was planning on combining it with Biomechanical Design and had not expected to graduate on a topic related to imaging. However after some courses, I felt that combining Biomechanical Design with Systems and Control was not the topic for me. Then I remembered I really enjoyed the filtering and identification course that Professor Verhaegen thought, so I made an appointment with him and he introduced me to some topics, including this one. That is how I arrived at the topic Phase Diversity for Blind Multi-Frame Deconvolution for my Master thesis.

I would like to thank my supervisor Prof.dr.ir M Verhaegen for introducing me to this topic, the notes and advise on my writing and the insightful questions during the group meetings. I would also like to thank my daily supervisor Dr. O.A. Soloviev, for motivating me during the thesis, for always responding fast to my questions, introducing me to interesting literature and reading the very early drafts of my thesis. I've laughed as at the start, when the group meetings were offline, he opened the group meetings with "Goodmorning Dominique and gentlemen". I got great motivation from those group meetings. It was nice to get and give feedback from/to fellow students graduating on similar topics and advising each other on interesting papers. Next I would like to thank Dr. N.J. Myers for being the third corrector on my graduation committee, while he is abroad.

Finally I would like to thank my cat Vlodewijk for teaching me to regularly make back-ups by crashing my computer, twice.

Delft, University of Technology
June 29, 2021

Dominique Vrijburg

Chapter 1

Introduction

When objects are imaged, often aberrations slip into the captured images. These aberrations can for example be introduced by the imaging system, turbulence in the atmosphere or by the measured sample [2, 3]. The aberrations can be modeled as a phase distortion at the aperture of the imaging system. The distortions can be removed with (additional) hardware, software or a combination of them. Using hardware, to remove the distortions induced by the imaging system, you can buy a "better", probably more expensive, lens. And to compensate for the turbulence or sample induced distortions an adaptive optical system can be added, with for example a deformable mirror. To control this mirror the incoming phase distortion has to be measured or predicted. Measuring can be done with a Shack-Hartman Sensor and for the prediction multiple algorithms exist. However including an adaptive optical system increases the costs and decreases the simplicity [4].

Another way to reduce the distortions in images is by post-processing them. If the aberrations and the object are both unknown, retrieving the aberrations and removing them from the image is called blind deconvolution [5]. Estimating both the object and the aberration from an image is an ill posed problem and is therefore dependant on *a priori* knowledge. To increase the information for blind deconvolution, multiple images can be used, this is also known as Blind Multi-frame Deconvolution.

Diversity imaging is a technique for Blind Multi-frame Deconvolution (BMFD). In diversity imaging a known perturbation is added from image to image. This diversity can be a perturbation in terms of amplitude (amplitude diversity), phase (phase diversity) or a different wavelength can be imaged (wavelength diversity) [6].

Wilding *et al.* [4] have shown that introducing phase diversity for BMFD can be used to improve the object reconstruction from the deteriorated images. To extract the object they used the Tangential Iterative Projection (TIP) algorithm [1] and they added the phase diversity with a deformable mirror. It sounds counter-intuitive to add even more aberrations to filter out other aberrations, but in their case it leads to a less distorted image after processing the images with TIP. The Phase Diversity (PD) can also be introduced with a different tool and reconstructed with a complimentary algorithm.

In literature mainly the phase aberration defocus is used as diversity [7, 8, 9]. One of the reasons for this is that it is easy to implement.

According to Smith [10] Defocus PD works for retrieving even-ordered aberrations such as astigmatism, but fails to retrieve odd-ordered aberrations as coma. This is because it is rotationally symmetric with respect to the optical axis. Smith looks into the channel capacity of the Modulation Transfer Function (MTF) of an imaging system in combination with a certain aberration. The goal was to use phase diversity, given this specific aberrations, to produce the best possible composite MTF. In terms of channel capacity of the MTF Smith concludes the optimal phase diversity is different, if a different aberrations is present. This optimal PD for a certain aberration has some utility, but more can be gained from compensating the known aberration directly.

Goal of this Research

In BMFD multiple types of diversities have been applied, like amplitude, phase and wavelength diversity [6]. This research will focus on Phase Diversity (PD). The focus on PD has been made, because PD has the advantage that no photons are blocked. This makes it more widely applicable, because it can be used in situations where few photons are present. In that case we expect it to outperform Amplitude diversity, as in [3]. In literature in general Defocus PD is applied in combination with BMFD.

As is mentioned in [10], if the MTF goes to zero or has a very low value at a certain frequency in the frequency spectra of all images, this frequency will not be represented in the images. Therefore it will not be possible to retrieve the information at that frequency. In this research we will try to design a PD that makes sure the low MTF frequencies are different for the different diversity images. Smith [10] looked into finding an optimal PD when a certain aberration was present based on the MTF. In this research we want create a PD that outperforms Defocus PD for all unknown aberrations, instead of finding the optimal one for a certain aberration.

Many algorithms for BMFD have constraints regarding the used diversity, information on the aberration or the aperture. The TIP algorithm [1] does not use knowledge about the aberrations as a constraint. Also this algorithm performs good with low Signal to Noise Ratio (SNR). Therefore in this research we will try to find a PD that improves the object reconstruction using TIP compared to Defocus PD. The quality of the reconstructions will be measured with two metrics, the Peak Signal to Noise Ratio (PSNR) and Structural Similarity (SSIM).

This problem has been split into two parts. In the first part we look into defining the PD before we even take any image. In the second part we already have some images and try to find a PD to add to next image that will be taken. This leads to the following research question: Research whether there is a phase diversity that leads to a reconstruction of the object using the TIP algorithm, with a higher PSNR or SSIM than Defocus PD. Two cases are considered, first the case where no information about the object or aberrations is present and no images have been taken yet, the PD is predefined. In the second case already some images have been taken and we look for the PD to add to the next image.

In the first part, where we predefine the PD before taking any images, two approaches will be used: some PD proposals will be inspired on (phase) diversities found in literature, others

will be based on the MTFs of an imaging system in combination with a certain PD.

In the second part, where already some images have been taken, in the frequency spectra of the collected images the frequencies that are poorly presented will be identified. With this information a MTF will be searched that enhances those frequencies.

Outline of the Thesis

In chapter 2 the basics of image formation and deterioration are explained. In chapter 3 (blind) deconvolution methods with a focus on the TIP algorithm will be explained. In chapter 4 existing (phase) diversities from literature will be discussed.

Next suggestions on new PD methods for Blind Multi-frame Deconvolution will be done. In chapter 5 we will propose PDs for the first case, where no images have been taken yet. In chapter 6 a method will be proposed for the second case, to determine what PD to add to the $N + 1^{th}$ image when already N images have been taken. The proposals in both these chapters will be tested in simulations. In chapter 7 the results will be discussed and recommendations for future research will be done.

This Master thesis project is performed for the master Systems and Control. The project is performed at the Delft Center for Systems and Control (DCSC), Delft University of Technology (TU Delft).

Notation

In this paper the following notation will be used in parameters and equations. Capital letters denote the 2D Fourier transform of the corresponding small letters, so H is the Fourier transform of h . A $*$ denotes convolution and \circ pointwise multiplication. \hat{H} denotes it is an estimate of H and H^* denotes it is the complex conjugate. In an image the pixel coordinates will be noted as $[x,y]$ and in the frequency domain as $[u,v]$. In images of the frequency domain the absolute value will be displayed. The frequency displayed in the center is zero and the higher frequencies are displayed at the edges.

Chapter 2

Image formation.

An object emits or reflects light that can be captured with for example a Charge Coupled Device (CCD) [11]. The light from the object will be modulated by the imaging system before it reaches the CCD. In this chapter will be explained how images are created and deteriorated mathematically. In the first section we will explain optical concepts to create an image of a point source. In the second section this will be expanded to imaging extended objects. In this chapter only monochromatic light will be considered.

2-1 Image of a point source

A point source emits light uniformly in all directions and is of negligible size. When the light emitted by a point source is captured, it will not be displayed as a perfect point in the image. The causes are the wavelike nature of light and deteriorations added mainly by the turbulence in the atmosphere, by the sample or by perturbations in the imaging system or [1, 2]. The waves of light emitted by the source can be described as wavefronts. The effects of deterioration can be modeled by a phase distortion $\phi(x)$ in this wavefront at the aperture. The description of the wavefront at the aperture is called the pupil function [1].

2-1-1 Pupil function

The pupil function $P(x, y)$ in Equation 2-1 describes the wavefront entering the aperture of the imaging system. It consists of the amplitude function $A(x, y)$ and the phase of the incoming wavefront $\phi(x, y)$ at the aperture. The amplitude function is usually binary function corresponding to the aperture and is 1 inside the aperture and 0 outside. The phase is proportional to the aberrated wavefront across the aperture.

$$P(x, y) = A(x, y)e^{i\phi(x, y)} \quad (2-1)$$

The unknown phase-aberration function $\phi(x, y)$ can be described for every pixel, but it can also be parameterized. Often this is convenient because it reduces the amount of unknown parameters.

Zernike Polynomials

One way to describe the phase of a wavefront is as a weighted sum of Zernike Polynomials. Zernike Polynomials are predefined polynomials and are particularly of interest when defining an arbitrary wavefront over a circular aperture. Noll [12] ordered the polynomials with a single index and that order is used in this paper. The first 15 Zernike Polynomials are described in Appendix A. In this appendix the ordering, name, formula and shape of the polynomials can be found. Equation 2-2 gives the relation between the wavefront aberrations ϕ and the Zernike polynomials.

$$\phi(x, y) = \sum_i a_i Z_i(x, y) \quad (2-2)$$

Where x and y are the aperture coordinates normalized from -1 to 1 inside the aperture of radius R . Z_i is the Zernike Polynomial of Nolls order i . The coefficient a_i determines the amplitude of Zernike polynomial i in the wavefront.

2-1-2 Distorted wavefront

The phase ϕ in the pupil function describes the distorted wavefront. In this thesis three types of aberrated wavefronts will be considered. These three aberration types are lower order aberrations, Kolmogorov phase screens and sparse phase aberrations.

Figure 2-1 a) shows a lower order phase aberration. In this research these are constructed from the first 15 Zernike Polynomials. The expressions for the Zernike polynomials can be found in Appendix A. The first 15 polynomials use expressions up until the fourth order. Figure 2-1 b) shows a Kolmogorov phase screen, these are used to model atmospheric wavefront distortions. More information on Kolmogorov phase screen can be found in [13].



Figure 2-1: Example of a) a Lower order, b) Kolmogorov and c) sparse aberrated wavefront.

In Figure 2-1 c) a sparse wavefront is shown. Like a sparse matrix it has mostly zero entries.

2-1-3 Amount of wavefront error

In this research to indicate how big the aberrations in the wavefront are, the Root Mean Square (RMS) and the Peak-to-Valley wavefront error are used. The RMS wavefront error is calculated as the standard deviation of the wavefront ϕ in the pupil function. It is expressed in units wavelength λ . The Peak to Valley wavefront error is the maximum error between the wavefront ϕ and a flat wavefront [14].

2-1-4 Point Spread Function

The observable of a point source is called the Point Spread Function (PSF)[15]. Because the deflection of the light by an ideal lens can be described with the Fourier transform, the Fourier transform is performed to get from the wavefront at the aperture to the image plane [15]. The imaging system captures the intensity of the field distribution and not the phase. Therefore the relation between the pupil function $P(x, y)$ and the PSF $h(x, y)$ is given by Equation 2-3.

$$h(x, y) = c \cdot |\mathcal{F}(P(x, y))|^2 = c \cdot \left| \mathcal{F} \left(A(x, y) e^{i\phi(x, y)} \right) \right|^2 \quad (2-3)$$

Here \mathcal{F} denotes the 2-Dimensional discrete Fourier Transform. The constant c normalizes the PSF such that the sum of all pixels is one. This is done because the intensity of the point source is in a way spread out over multiple pixels and all together they should sum up to the original value. The PSFs of an aperture with as aberration one of the first 15 Zernike Polynomials, can be found in Appendix A. The shape and size of the aperture influence the shape of the PSF. When there are no phase aberrations present, the PSF and image are called diffraction limited. The diffraction limited image is however not equal to the object and the PSF is not a single pixel.

2-2 Image of an extended object

An extended object can be seen as a combination of point sources with different intensities. The object is split into N by M pixels, that are treated as point source with different intensities. When the illumination is incoherent, the contribution of each point source can be linear superpositioned to form the image [16]. When the wavefront emitted by every point source is deteriorated in the same way when it arrives at the aperture, the image contains isoplanatic aberrations. This is explained in the next subsection. When the deteriorations for the different "point sources" differ, the object has anisoplanatic aberrations. The focus in this paper is on isoplanatic aberrations.

For isoplanatic aberrations the PSF can be seen as the impulse response function of one point source [15]. To create the image of an extended object we convolve the object with the PSF. The noise in the image is added as $e(x, y)$. The convolution is described by Equation 2-4.

$$i(x, y) = \sum_p \sum_q o(x, y) h(p - x + 1, q - y + 1) + e(x, y) \quad (2-4)$$

$$i(x, y) = o(x, y) * h(x, y) + e(x, y)$$

In this equation $[p,q]$ are the pixels in the PSF, $*$ denotes convolution and $e(x,y)$ is the noise in pixel $[x,y]$. An example of the convolution and noise addition with an object is shown in Figure 2-2.

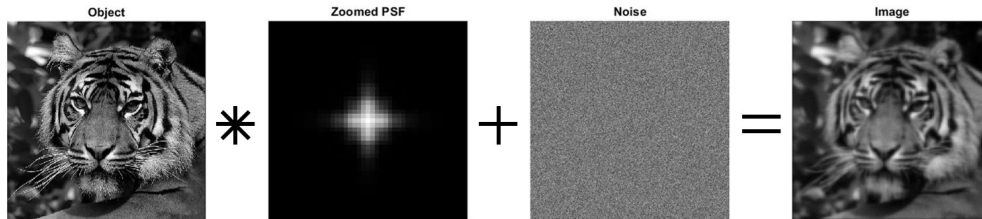


Figure 2-2: Image formation with an isoplanatic aberration. The object, PSF and noise leading to the image displayed on the right are displayed. The noise is gaussian with $\sigma = 0.01$ and normalized from 0 to one in the image. The PSF is zoomed with factor 12 and also normalized in this figure.

Frequency domain

Convolution in the spatial domain is equal to pointwise multiplication in the frequency domain. Therefore the Fourier transform of the object, PSF, noise and image are taken. The Fourier transforms are denoted with capital letters. The formation of the image in the frequency domain is described in Equation 2-5.

$$I(u, v) = O(u, v) \circ H(u, v) + E(u, v) \quad (2-5)$$

Here \circ denotes pointwise multiplication. In the frequency domain, the high frequencies are given towards the edges of the transformed image and the low frequencies at the center. When the Fourier transform of the PSF, the Optical Transfer Function (OTF) $H(u, v)$, is zero at a certain frequency (u,v) , this frequency will also not be present in the image of the object. In the next chapter multiple methods to reconstruct the original object from the captured images are discussed.

Deconvolution methods in imaging

The formation of an image by convolving the object with the Point Spread Function (PSF) and adding the noise was described in the previous chapter (Equation 2-4). In this chapter several methods will be explained to restore the object from one or multiple images. First deconvolution methods with a known PSF are discussed. When the PSF is unknown, blind deconvolution is used, this is an ill-posed problem because it has no unique solution, so it is dependent on the *a priori* knowledge. To obtain more information for blind deconvolution, multiple images can be used, this is called Blind Multi-frame Deconvolution (BMFD). Algorithms to perform Blind (Multi-Frame) Deconvolution are explained at the end of this chapter.

3-1 Deconvolution with a known PSF

In this section, three deconvolution filters will be introduced to restore the object with a known PSF. We will start with the inverse filter [17]. Next the Wiener filter [18], based on the minimizing the mean square error, and the Tikhonov Miller filter [16], using regularization, will be introduced to restore the object.

3-1-1 Inverse Filtering

A naive way to restore the object from the image is dividing the Fourier transform of the image by the PSFs. This is called inverse filtering and is given in Equation 3-1[17].

$$\hat{o} = \mathcal{F}^{-1} \left\{ \frac{I}{\hat{H} + \epsilon} \right\} = \mathcal{F}^{-1} \left\{ \frac{O \circ H + N}{H + \epsilon} \right\} \quad (3-1)$$

In this equation ϵ is a small constant that prevents division by zero. As can be seen from the equation, when H goes to zero at frequency (u,v) , the noise will be amplified with a factor $\frac{1}{\epsilon}$. An example of the restoration of an object with this inverse filter with $\epsilon = 0.01$ can be seen in Figure 3-1 for both an image without (3-1 d.) and with (3-1 g.) added gaussian noise.

3-1-2 Wiener Filter

To estimate the object with the smallest Mean Squared Error (MSE) the Wiener Filter is used. The MSE is explained in section 3-4.

When the noise is signal independent, to estimate the object with a linear filter, minimizing the MSE leads to the Wiener filter given in Equation 3-2 [18].

$$W_{wiener} = \frac{H^*}{H^*H + \frac{S_{nn}}{S_{jj}}} \quad (3-2)$$

In this equation S_{nn} and S_{jj} represent respectively the noise and object power spectra. The object estimation using the wiener filter is given by.

$$\hat{o} = \mathcal{F}^{-1}(W_{wiener}I) = \mathcal{F}^{-1}\left(\frac{H^*I}{H^*H + \frac{S_{nn}}{S_{jj}}}\right) \quad (3-3)$$

At the frequencies where H is zero, \hat{O} will also be zero. Therefore a linear Wiener filter can only restore the image within the frequency range of the PSF [18]. When the power spectra are unknown, the modified wiener filter substitutes $\frac{S_{nn}}{S_{jj}}$ by a small constant ϵ . An example of the restoration of an object with this wiener filter with $\epsilon = 0.0025$ can be seen in Figure 3-1 from an image without (e.) and with noise (h.).

3-1-3 Tikhonov Miller filter

Another filter for image restoration is based on the least squares solution. The least squares error is given below.

$$\|H \circ \hat{O} - I\|^2 \quad (3-4)$$

In this equation $\|\cdot\|$ denotes the euclidean norm. Directly minimizing this equation does not find the correct object, since the (higher order) frequencies that are not present in the PSF will also be filtered out of the solution. Therefore this is known as an ill-posed problem.

To find a better estimate of \hat{o} , Tikhonov regularization can be applied. [16, 19, 18].

$$\Phi(\hat{o}) = \|H \circ \hat{O} - I\|^2 + \lambda \|C\hat{o}\|^2 \quad (3-5)$$

In this equation λ and C are the regularization parameter matrix. The first part of the function is a MSE fit and the second part is a regularization based on an energy bound [18]. This results in the Tikhonov Miller solution (TM).

$$W_{TM} = \frac{H^*}{H^*H + \lambda C^*C} \quad (3-6)$$

This solution is equal to the Wiener filter in Equation 3-2 for $\lambda C^*C = S_{nn}/S_{ff}$. An example of the restoration of an object with this Tikhonov Miller filter for an image with and without noise can be seen in Figure 3-1. The regularization parameter is set to the generalized cross validation [20] which is in this example $7 \cdot 10^{-4}$ for the noise free image and 0.02 for the image with noise.

3-1-4 Comparison of the Inverse, Modified Wiener and Tikhonov Miller filter

In Figure 3-1 we can see the effect of the different deconvolution methods on two example images. Both example images have been created convolving the same object (Figure 3-1a) and same PSF (3-1b), only to the second image noise with $\sigma = 0.01$ is added. This second image is shown in Figure 3-1c. In the second row in this figure (3-1 d, e, f) we see the noise-free image deconvolved with respectively the Inverse, Wiener and Tikhonov-Miller filter. In the third row (3-1 g, h, i) we see the deconvolutions of the image with noise. For the six estimations of the object, the Peak Signal to Noise Ratio (PSNR) and Structural Similarity (SSIM) are given. These error metrics will be explained in section 3-4. For both metric applies, a higher value means the restoration is more equal to the object.

For both the image with and without noise, the inverse filter has the lowest PSNR and SSIM. Especially when there is noise (3-1 g) we see amplification of it, which decreases the error metrics a lot. The modified Wiener and TM filter, have a much higher PSNR and SSIM. They both improve in the similarity of the reconstruction in comparison to the constructed image. The differences between those filters are determined by the choice of ϵ for the modified Wiener filter and the regularization parameters in the Tikhonov-Miller filter.

3-2 Estimating the wavefront from the PSF

From a PSF the wavefront can be estimated, this is called phase retrieval. The Gerchberg Saxton algorithm is a phase retrieval algorithm that lies on the basis of many Blind (Multi-Frame) Deconvolution algorithms [7]. The algorithm estimates the wavefront at the aperture from a PSF measurement and the known aperture of the lens [8]. It is an iterative algorithm that iterates between the measured PSF and the Optical Transfer Function (OTF).

As described in subsection 2-1-1 the phase ϕ of the wavefront can be parameterized with for example Zernike polynomials. Gonsalves [2] used the minimum square error between the measured PSF and the constructed PSF from the estimated phase $\hat{\theta}$, as a metric to minimize. The metric is minimized over the coefficients a_i of the parameterization. Details on this algorithm can be found in Ref. [21]. Given that the detector noise is Gaussian, the estimated phase is a maximum likelihood estimation of the real phase.

3-3 Blind multi-frame deconvolution for extended objects using Phase Diversity

When the PSF is unknown, both the object and PSF need to be estimated. Deconvolving two unknown signals is called blind deconvolution [5]. This is an highly undetermined problem and optimization algorithms can often get trapped in local minima. It may be necessary to include constraints from *a priori* knowledge, to get to an unique solution [19]. By taking multiple images, more information on the object can be gained. Using this is called Blind Multi-frame Deconvolution (BMFD). A technique in BMFD is Phase Diversity.

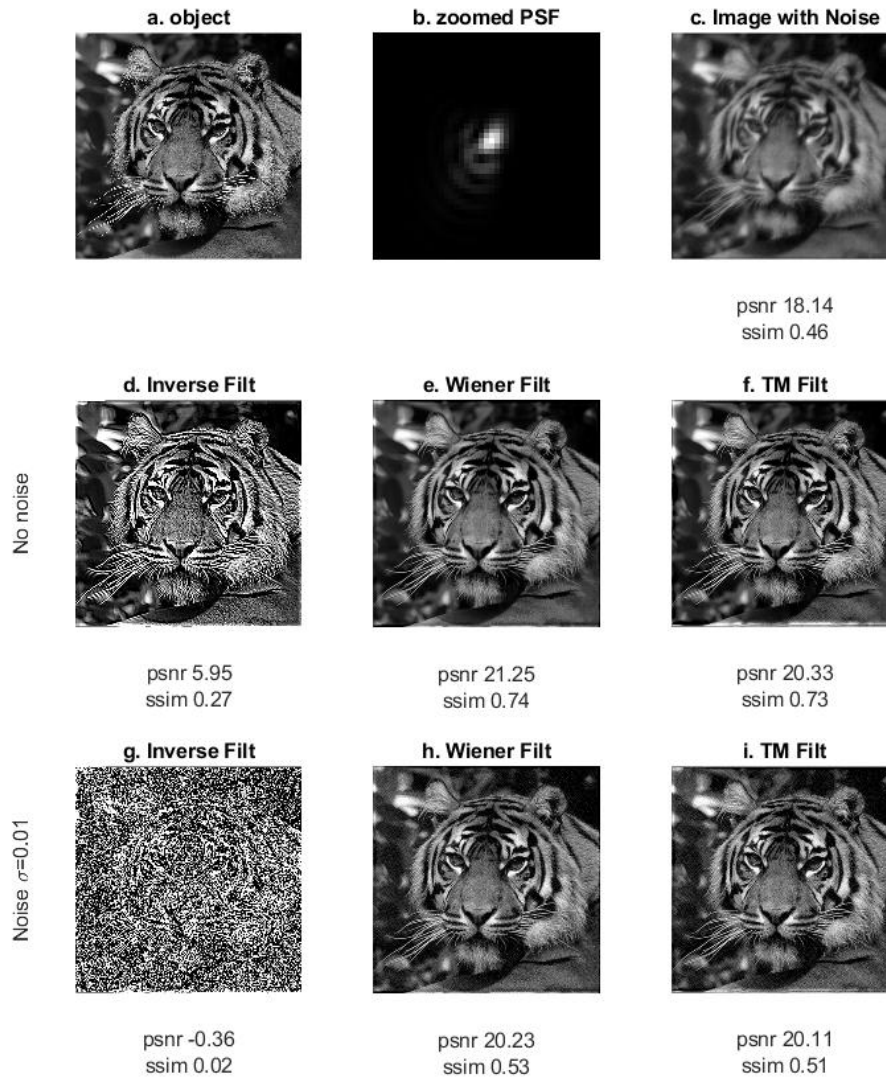


Figure 3-1: An example of object restoration with different deconvolution methods. In (a.) we see the original object. (b.) shows the PSF used to create the image. In (c.) the image were noise with $\sigma = 0.01$ was added is shown. In (d,e,f) we see the estimated object after deconvolution of the noise free image with respectively the inverse, modified wiener and Tikhonov Miller filter. In image (g,h,i) deconvolution with the same filters was performed on the image with noise. The PSNR and SSIM of images (c-i) with respect to the original object in (a.) is given below each image.

3-3-1 Blind Multi-frame Deconvolution using knowledge on Phase Diversity

The joint estimation of object and phase aberration is done by Gonsalves using two images of the same object. For the second image, a known phase θ is added to the pupil function Equation 2-1. This leads to a description of the two PSFs as follows:

$$\begin{aligned} h_1(x, y) &= c \cdot \left| \mathcal{F} \left(A(x, y) e^{i\phi(x, y)} \right) \right|^2 \\ h_2(x, y) &= c \cdot \left| \mathcal{F} \left(A(x, y) e^{i\phi(x, y) + i\theta(x, y)} \right) \right|^2 \end{aligned} \quad (3-7)$$

Adding phase to create differences between multiple images is called Phase Diversity (PD) [6]. Gonsalves used Defocus PD, in chapter 4 different diversities will be discussed. To optimize the reconstruction of the object, Gonsalves uses the following error metric in his optimization [2]:

$$E = \int [I_1 - \hat{O} \circ \hat{H}_1]^2 dx + \int [I_2 - \hat{O} \circ \hat{H}_2]^2 df \quad (3-8)$$

In which $I_{1,2}$ and \hat{O} are the fourier transformers of the two acquired images and the estimated object, $\hat{H}_{1,2}$ the estimated OTFs. When minimizing the error E in the frequency domain, using Parseval's theorem Gonsalves got the next expression for his estimated Fourier Transformed object:

$$\hat{O} = \frac{\hat{H}_1^* I_1 + \hat{H}_2^* I_2}{|\hat{H}_1|^2 + |\hat{H}_2|^2} \quad (3-9)$$

The * denotes the complex conjugate and the ^ denotes that it is an estimate. The expression for \hat{O} is substituted into the error metric, which then is only dependent on the OTFs.

Paxman, Schultz and Fienup look into the PD technique using maximum likelihood estimation. For additive Gaussian noise, their objective function is a generalization of Gonsalves' objective function. However when Poisson noise is present, no closed form expression for the object could be found. More information on their algorithm can be found in [7].

3-3-2 Tangential Iterative Projection algorithm

In many BMFD algorithms, the differences between the images taken were only caused by the *known* phase difference in the pupil function, leading to two different PSFs as in Equation 3-7. Also this knowledge on the diversity was used to reconstruct the object and wavefront. A different BMFD algorithm is the Tangential Iterative Projection (TIP) algorithm [1]. Multiple images of the same object with different (temporal) aberrations are taken, so now the differences in phase from image to image are unknown. From the acquired images it retrieves the unknown object and the PSFs. So in contrary to the previously explained algorithms it does not retrieve the wavefront. The goal of the algorithm is to derive a minimum for the least squares problem in Equation 3-10.

$$\begin{aligned} \{\hat{H}_n, \hat{O}\} &= \arg \min_{H_n, O} \sum_{n=1}^N \|I_n - O \circ H_n\|^2 \\ s.t. \quad O &\in \mathcal{O} \\ H &\in \mathcal{H} \end{aligned} \quad (3-10)$$

This algorithm does not optimize the minimization problem, it modifies this problem to get an estimate of the object with simple operations and little *a priori* knowledge.

As *a priori* knowledge a feasible set for the object o and the PSFs h_n are set. Both are non-negative. The object pixels range from 0 to 1 and the PSF sums to one. For the PSF a maximum size is set. The feasible sets are denoted as respectively \mathcal{O} and \mathcal{H} .

At the start of the algorithm the PSFs h_n are set to an initial value. In the iterative process first the linear multi-frame deconvolution filter in Equation 3-11 estimates the object. This estimation is equal to the one from Paxman *et al.* in [7] with the addition of ϵ in the denominator to prevent division by zero.

$$\hat{o} = \mathcal{F}^{-1} \left\{ \frac{\sum_{n=1}^N (H_n)^* \circ I_n}{\sum_{n=1}^N |H_n|^2 + \epsilon} \right\} \quad (3-11)$$

The subscripts n denote a parameter corresponds to the n^{th} diversity image. Next, the estimated object is projected on the feasible set \mathcal{O} . Using the Fourier transform of the feasible object, now single-frame linear deconvolution is used to update the estimates H_n . The linear deconvolution is shown in Equation 3-12. It is similar to the inverse filter in Equation 3-1.

$$\hat{h}_n = \mathcal{F}^{-1} \left\{ \frac{I_n}{\hat{O} + \epsilon} \right\} \quad (3-12)$$

The estimated PSFs \hat{h}_n are projected on the feasible set \mathcal{H} . The next iteration now starts from the first step where the object is estimated. The number of iterations is set beforehand. A visualisation of the steps in the algorithm is displayed in Figure 3-2.

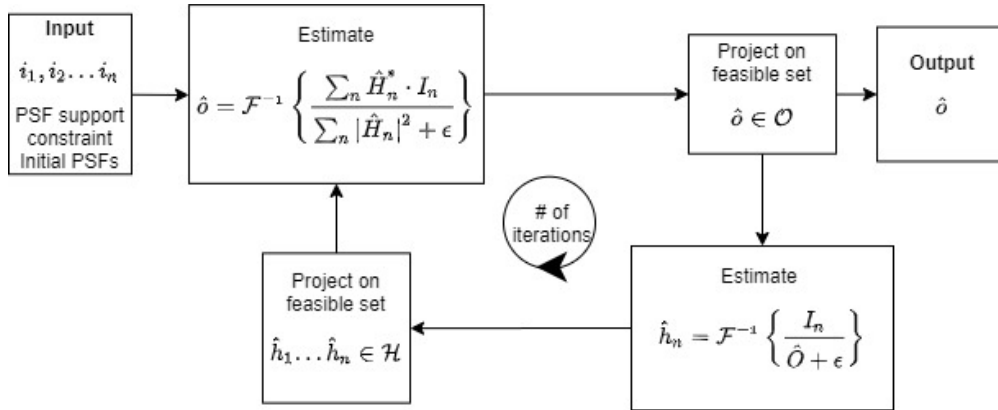


Figure 3-2: A visualisation of the steps in the TIP algorithm [1].

Single frame TIP

The authors of the TIP algorithms also modified it to make it applicable to single frame blind deconvolution [22].

.

3-4 Quality of the restored object

To compare the performance of the different object reconstruction methods, different metrics can be used. There are metrics that look pixel by pixel at the error between the object and reconstruction, like the PSNR. Other metrics calculate a value that resembles the visual perception of the human, like the SSIM. In this section we will explain some metrics that are used in imaging.

3-4-1 MSE and PSNR

The Mean Square Error (MSE) is a metric that calculates the difference between the two images for every pixel, the difference between the pixels is squared and then summed up. The equation is shown in 3-13 [23].

$$MSE(i_1, i_2) = \frac{1}{NM} \sum_{x=1}^N \sum_{y=1}^N [i_1(x, y) - i_2(x, y)]^2 \quad (3-13)$$

In this equation i_1 and i_2 are the two images to compare, both containing $M \times N$ pixels. The MSE has simple, not heavy, calculations. A high value for the MSE means that the error is bigger, so for a better resemblance between the object and restoration a lower MSE is necessary.

The PSNR is closely related to the MSE and is shown in Equation 3-14. There are three differences. Firstly, the unit is dB. Secondly, the PSNR includes the dynamic range L of the images. So the dynamic range does not influence the quality metric. Thirdly, it is inverse so a higher PSNR means a better resemblance between object and reconstruction[23].

$$PSNR(i_1, i_2) = 20 \log_{10} \left(\frac{L^2}{MSE} \right) = 20 \log_{10} \left(\frac{L^2 MN}{\sum_{x=1}^N \sum_{y=1}^N [i_1(x, y) - i_2(x, y)]^2} \right) \quad (3-14)$$

Both the MSE and PSNR are simple and have a clear physical meaning, but they do not resemble the visual perception of the human.

3-4-2 SSIM

The structural similarity (SSIM) is a metric based on the visual perception of the human and is shown in Equation 3-15 [23, 24].

$$SSIM(i_1, i_2) = \frac{(2\mu_1\mu_2 + c_1)(2\sigma_{12} + c_2)}{(\mu_1^2 + \mu_2^2 + c_1)(\sigma_1^2 + \sigma_2^2 + c_2)} \quad (3-15)$$

Where $\mu_{1,2}$ are the local means of respectively image 1 and 2, these are used to compare the luminance of the images. The standard deviations $\sigma_{1,2}^2$ are used to compare the contrast. The structure is compared using σ_{12} , the co-variance. c_1 and c_2 are constants depending on the dynamic range. A higher value for the SSIM means a better reconstruction of the object for this metric.

3-4-3 Sharpness

The sharpness is a metric that does not depend on an reference object. It indicates the amount of small detail that can be seen in the image. There are multiple equations for sharpness, in Equation 3-16 a simple formula depending on the gradient is shown [25].

$$Sharpness(i_1) = \sum_{x=2}^N \sum_{y=2}^M \frac{\sqrt{(i(x,y) - i(x-1,y))^2 + (i(x,y) - i(x,y-1))^2}}{N-1} \quad (3-16)$$

The magnitude in both x and y direction is summed over all pixels to derive the sharpness. A higher value indicates a sharper image.

3-4-4 Comparison of the metrics

In Figure 3-3 examples of an object with different deteriorations are shown. The PSNR and SSIM with respect to the object are calculated and the sharpness of the images is calculated. The corresponding metric values can be found in Table 3-1. The Gaussian noise in Figure 3-3 b) and i) have a standard deviation of $\sigma = 0.1$. In the contrast in Figure 3-3 d) mostly the medium bright pixels are darkened. In 3-3 e) each pixel value of the object is replaced by its square root, this makes mostly the medium bright values brighter.

image	PSNR	10· SSIM	10·Sharpness
a) Obj	–	–	0.74
b) Gaussian noise	20.60	5.21	1.17
c) Salt&Pepper	17.64	5.38	1.11
d) Contrast top	15.08	6.36	0.53
e) Contrast bottom	13.73	7.39	0.74
f) Defocus small	19.32	5.63	0.21
g) Defocus big	16.09	3.32	0.09
h) Random PSF	16.64	3.71	0.11
i) Random PSF+noise	16.64	0.88	0.90

Table 3-1: Different quality metrics for the images in Figure 3-3. The green values represent the best value for a certain metric and the red value the worst.

For the different metrics in Table 3-1, the highest and lowest value for that metric have been highlighted respectively green and red. A few values catch the eye. The image with adjusted contrast in Figure 3-3 e) is the "worst" image according to the PSNR and the "best" when looking at the SSIM. The other image with adjusted contrast (3-3 d)) has similar values. This can be explained by the fact that the SSIM looks locally at the image and the PSNR at the entire image at once.

For the sharpness a thing to notice is that some deteriorated version of the object have a higher sharpness than the object itself. This are the images where noise is added (3-3 b, c, i). The noise here increases the gradient from pixel to pixel. Because noise being present in the

image leads to a higher Sharpness, this metric will not be used to compare the reconstructions in the following chapters.



Figure 3-3: The object at the top with several deteriorated versions below. The PSNR, SSIM and Sharpness of the different images can be found in Table 3-1.

Diversity Methods in Literature.

In the previous chapter different Blind Multi-frame Deconvolution (BMFD) algorithms were discussed. For this multiple images are necessary, with different aberrations present. For some algorithms the difference between the aberrations have to be known ([7, 2]), while for other algorithms they do not [1]. When the aberrations in the wavefront are time-variant, one can take multiple images over time to capture images with different PSFs. When the aberrations do not change over time, the wavefront has to be adjusted from one image to another. This change in aberrations is called diversity. Paxman [6] mentions multiple forms of diversity, phase, wavelength and translation diversity. Wilding *et al* [3] use amplitude diversity. In this chapter both diversity shapes used in BMFD, as pupil design used in other imaging applications are described. First some different purposes of diversity will be mentioned and next examples of diversity shapes will be explained.

4-1 Purpose of Diversity

Diversity is applied in various fields. For a three-dimensional fluorescent microscope, Wilding *et al.* [3] were able to retrieve certain frequencies by adding diversity, that they did not retrieve without the diversity. Gonsalves [8] and Paxman [7] already mentioned adding a known amount of defocus to create two different images because Defocus Phase Diversity (PD) is easy to implement. Dean and Bowers [9] also use Defocus PD, but they want to recover the dominant spatial frequency component in the wavefront for a point source. Sharma *et al.* [26] want to be able to recover (pure phase) extended objects from two images, and propose spiral phase diversity for that. Smith [10] and Miyamura [27] tried to optimize phase diversity for BMFD. Shechtman *et al.* [28] did not perform (blind) deconvolution but want to find the location of a 3D positron emitter and design a phase mask for that. Another purpose of adapting the Point Spread Function (PSF) is to create an extended depth of field for deconvolution [29]. Previous examples all focused on monochromatic light. Yang *et al.* made use of the different wavelengths in poly-chromatic light to improve the image quality. Depending on their purpose, they all designed different adaptations of the pupil function in Equation 2-1. In this chapter we will give examples of those different diversities.

4-2 Examples of Diversity in Literature.

In this section multiple examples of diversity methods found in literature are discussed. First amplitude diversity is discussed. Amplitude diversity is very easy to implement since part of the aperture can just be blocked. However blocking light is undesirable when the signal is already weak compared to the noise, because even less photons can be caught with the imaging system. Therefore next, Phase Diversity (PD) is discussed because there no photons are lost. However it is often more difficult to add a mask that adds the desired phase addition than an amplitude mask. In the final section wavelength diversity will shortly be mentioned.

4-2-1 Amplitude Diversity.

For amplitude diversity, in the pupil function Equation 2-1 the amplitude function $A(x, y)$ is adjusted by adding a mask. In practice this means light passing through part of the aperture is blocked.

Amplitude Diversity with a Rotating Disk

Wilding *et al.* [3] increase the resolution of a three-dimensional fluorescent microscope by using amplitude diversity. The binary amplitude mask is created by a rotating disk. The disk can be seen at two different angles in Figure 4-1. The PSFs corresponding to the aperture amplitude functions are given in the same figure, there are no phase aberrations present in this example.

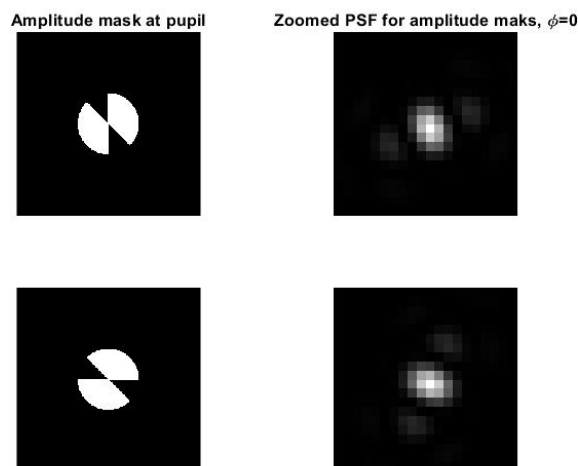


Figure 4-1: On the left the Amplitude mask of the Rotating Disk at two different angles, on the right the corresponding PSF when there are no phase aberrations present. For the PSF the 7% lowest frequencies are shown.

As can be seen, the PSF rotates with the same angle as the disk.

Wilding *et al.* used eight images to reconstruct the object. For every image the disk was rotated $\frac{\pi}{4}$ radians. The object was reconstructed using a recursive version of the Tangential

Iterative Projection (TIP) algorithm explained in subsection 3-3-2, more information on this algorithm can be found in [3]. With this amplitude diversity they could restore lost spatial frequencies.

4-2-2 Phase Diversity

Now different shapes of PD will be discussed. For PD we add a phase θ to the unknown phase ϕ of the wavefront in the pupil function. Changing the phase can be done using a deformable mirror or for example by inserting a transparent mask with a different refractive index. The advantage of phase diversity is that no photons are lost, which does happen when blocking the light with amplitude diversity. This advantage is especially important when the Signal to Noise Ratio (SNR) is low. For the different PDs we will start with Defocus PD which is most found in literature because it is easy to obtain. Next the addition of a spiral and saddle point phase patterns are discussed. Then the Cubic phase pattern that is used to create an extended depth of field is explained.

Defocus Phase Diversity

Defocus is a quadratic phase error that can be added, and is mainly used as PD in literature. Introducing Defocus PD is simple because it only needs a translation of the detector along the optical axis. One can take multiple images sequentially at different distances when the aberrations are time invariant, or use a beam splitter with a second detector. Paxman et al. [7] mentioned defocus as an example of PD for a BMFD algorithm in the previous chapter.

B.H. Dean and C.W. Bowers [9] predicted optimal diversity values for Defocus PD. To retrieve the aberration around a certain frequency, Dean tried to create maximum contrast in the PSF. Dean described the PSF of a point source when the wavefront has a sinusoidal phase aberration and defocus with amplitude a .

To obtain maximal contrast in the intensity measurements of the PSF, the theoretically optimal amount of Defocus PD is given by a_{max} in Equation 4-1 for the dominant spatial frequency v_0 . The amount of Defocus PD for minimal contrast is given by a_{min}

$$\begin{aligned} a_{max} &= \pm \frac{\lambda v_0^2}{(2k \mp 1)} \\ a_{min} &= \pm \frac{\lambda v_0^2}{2k} \end{aligned} \quad k = 0, 1, 2, \dots \quad (4-1)$$

In general aberrations do not consist of only one frequency, for the optimal amount of Defocus PD the dominant spatial frequency v_0 is used in the calculation. Dean determined the dominant spatial frequencies for the different Zernike modes. For lower dominant spatial frequencies, lower amounts of defocus should be used.

Spiral Phase Diversity

Sharma *et al.* [26] used spiral phase diversity to reconstruct (pure phase) objects from two images. In this research the unknown aberrations ϕ stayed constant and for the second image a known spiral phase θ was added as PD, the PD θ can be seen in Figure 4-2.

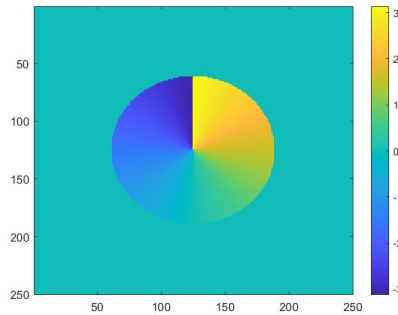


Figure 4-2: The spiral phase mask from Sharma[26].

Using a modified version of the Gergberg Saxton algorithm Sharma tried to reconstruct the complex amplitudes of the object from the two intensity measurements. The aperture of the imaging system was known and used as a constraint.

Using the spiral phase diversity and this algorithm, both objects of amplitude and phase could be reconstructed using 200 iterations. The spiral PD had a lower L2 error norm than when Defocus PD was used with this modified Gergberg Saxton algorithm.

Saddle Point Phase Diversity

Shechtman *et al.* [28] researched PSF design to find the maximal physical information about the 3D position of an emitter. To find this optimally informative PSF the mean of the $\sqrt{\text{CRLB}}$ over x-, y- and (in a limited range) z-position is minimized. The phase of the pupil function that lead to the optimally informative PSF was considered a free design parameter consisting of the first 55 Zernike polynomials. No unknown aberrations were present.

When the z position range was limited from -1.5 to 1.5 μm this resulted in a so called saddle point phase pattern as optimally informative. An approximation of this phase pattern and its PSF is displayed in Figure 4-3. For the estimation of the x and y position they look at the Center of Mass of the PSF. As can be seen in Figure 4-3, the PSF changes in shape when it is out of focus differently at both sides of the focal plane.

When the z range was 6 μm , the optimized phase pattern was called the 'cat mask', it can be found in the supplemental material of [28].

Cubic Phase Diversity

In [29] Dowski proposed a cubic phase mask to create an extended depth of field. An extended depth of field is wanted when all aberrations except for the amount of defocus are known. A

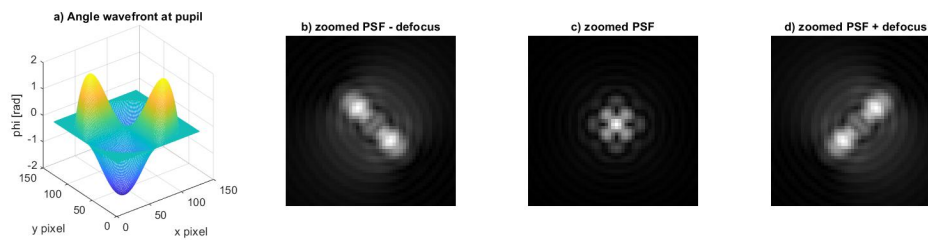


Figure 4-3: An approximation of the optimally informative saddle point phase pattern with in and out of focus PSFs. In a) the approximation of the phase pattern is given as a combination of the 5th and 12th Zernike polynomial. In c) the PSF of the phase pattern in focus is . Images b) and d) represent the PSF with defocus on either side of the focal plane.

cubic PD had an ambiguity function that was not depending on the amount of defocus. The derivation of the cubic phase can be found in [29]. From a single image, using a simple digital inverse filter the object can be reconstructed without having to know the amount of defocus. The cubic phase mask can be found in Figure 4-4 with its corresponding PSF independent of a large range of defocus.

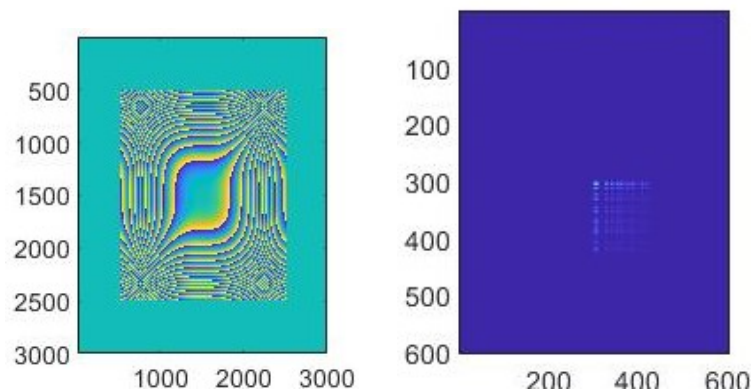


Figure 4-4: On the left the cubic phase mask from [29]. And on the right the corresponding PSF.

In 2007 Yang *et al.* [30] proposed an exponential phase mask for the same purpose. The advantage of their mask is that it has two free variables to construct the mask, which makes it more variable.

4-2-3 Wavelength diversity

So far we looked at monochromatic light. When poly-chromatic light is used, wavelength diversity is also an option [31, 6]. In [31] Yang *et al.* split the incoming light in two wavelength diversity channels with respectively wavelength λ_1 and λ_2 . Because both images are taken at the same time instance, the aberrations can be related as follows: $\phi_1 = \phi/\lambda_1$, $\phi_2 = \phi/\lambda_2$. The

phase aberration ϕ is parameterized with Zernike polynomials as described in Equation 2-2. In reconstructions the Tikonov regularized least squares problem with two wavelengths is minimized, like in subsection 3-1-3. Using one image and splitting it in two wavelength diversity channels improved the image resolution.

4-3 Determining diversity based on aberrations

At the moment in literature mainly Defocus PD is used in BMFD. M. Smith [10] and Miyamura [27] look into using different Zernike based Phase Diversities.

4-3-1 Optimizing the channel capacity

M. Smith [10] stated that since Defocus PD is rotationally symmetric, Defocus PD is effective in restoring even-order aberrations but will not work on odd-order ones, such as coma. In [10] quadratic and non rotationally symmetric PDs in comparison to using Defocus PD is researched. Smith looked into the channel capacity of the Modulation Transfer Function (MTF) of an imaging system in combination with a certain aberration. The goal was to find a phase diversity, given this specific aberrations, to produce the best possible composite MTFs. In this research the aberrations consist of a single Zernike mode. The phase diversity was made up of a single Zernike mode as well. Two sets of possible Zernike modes were looked at, lower order (4, 5, 6, 9, and 10) and higher order (14, 15, 20, 21, 27, and 28) Zernike modes. In terms of channel capacity of the MTF Smith concluded in general the lower order modes outperformed the higher order modes. Also the optimal phase diversity is different, when a different aberration was present. There is some utility in using this phase diversity when the aberration is known, but more can be gained from compensating the known diversities directly. However this research did not consider combinations of Zernike modes for either the aberration nor the PD. Furthermore it concluded the optimal PD was different when a different aberration is present, but it did not check whether there was a PD that outperformed Defocus PD for all aberrations without being optimal.

4-3-2 Optimizing Phase Diversity for a neural network

Miyamura [27] wanted to use a neural network to estimate a wavefront from multiple images of an extended object. The wavefront ϕ consists of certain known Zernike polynomials, but the amplitude of each polynomial is unknown. The metric in Equation 4-2 is used to determine which diversity images are necessary to retrieve the amount of those Zernike modes in his aberration.

$$M_n(u, v) = \frac{|I_0(u, v)|^2 - |I_n(u, v)|^2}{|I_0(u, v)|^2 + |I_n(u, v)|^2} = \frac{|H_0(u, v)|^2 - |H_n(u, v)|^2}{|H_0(u, v)|^2 + |H_n(u, v)|^2} \quad (4-2)$$

In this equation I_0, H_0 correspond to the Fourier transform of the image and Optical Transfer Function (OTF) without diversity and I_n, H_n to the one of the n^{th} diversity image. When one of the amplitudes a_i of a Zernike polynomial in the unknown phase ϕ changes, the metric should change with it. When this did not happen for a certain Zernike polynomial, an

additional diversity image was added for which it did change. Like Smith Miyamura assumed to have certain knowledge about the aberrations and only looked into using a single Zernike mode as PD instead of combining them.

4-4 Conclusions

When comparing amplitude diversity to Phase Diversity (PD), PD has the advantage that no photons are blocked. This makes it more widely applicable, because it can be used in situations where few photons are present. In that case we expect it to outperform amplitude diversity, like in section 4-2-1. In the following chapters monochromatic light will be assumed so wavelength diversity will not be an option.

In literature in general Defocus PD is applied in combination with BMFD [8, 7, 9]. Smith [10] looked into the channel capacity of the MTF of an imaging system in combination with a certain aberration. The goal was to use phase diversity, given this specific aberrations, to produce the best possible composite MTF. Smith concluded the optimal phase diversity is different, when a different aberration is present. However Smith did not check whether certain PDs did outperform Defocus PD without being optimal for that aberration. Also Smith did not consider combinations of PDs or other wavefront errors, only aberration and PDs consisting of a single Zernike mode were investigated. So in the following chapter new PD shapes are proposed. Part of them are inspired on shapes found in literature. Part of them are PDs that are based on the MTF, but now they will not be designed for a specific aberration but we will check whether there is one that outperforms Defocus PD for all aberrations.

Predefined Phase Diversity for Blind Deconvolution

In the previous chapter we discussed some existing examples of (phase) diversity. In this chapter new Phase Diversity (PD) combinations are proposed. In this chapter we determine the PD before any images are captured.

In the first section three new PD shapes that are inspired on shapes found in literature are proposed. This are the rotating phase PD, the rotating half phase PD and the spiral PD. In the next section new PDs that are based on optimizing the Modulation Transfer Function (MTF) over the PD are proposed and explained. They will not be designed for a specific aberration as in section 4-3, but we will investigate whether there is one that outperforms defocus for all aberrations.

5-1 New Phase Diversity Shapes based on Shapes in Literature

In this section three PDs are proposed that are inspired on diversities found in literature. In section 4-2-1 the amplitude diversity with the rotating disk was discussed. Here a rotating phase PD is proposed as first new PD. Also inspired on this diversity, we propose the rotating half phase PD. In section 4-2-2 a spiral phase mask was proposed in combination with an image without additional phase. They combined this with a modified Gergberg Saxton algorithm. We propose ta combination of rotated spiral phases as PD and investigate if it leads to an increased reconstructions quality with the Tangential Iterative Projection (TIP) algorithm.

5-1-1 Rotating phase Phase Diversity

The rotating phase is a PD based on the amplitude diversity in section 4-2-1. For the rotating phase PD, at the aperture a phase θ is added at the same locations as where the rotating disk

blocked the amplitude in section 4-2-1. A visualization of this is shown in Figure 5-1. Where the image is black, the amplitude is zero. Where the image is white or blue, the amplitude is one. At the blue wedges, a phase θ is added to the wavefront at the aperture. For every image taken the phase mask is rotated by 45 degrees. This diversity is proposed because

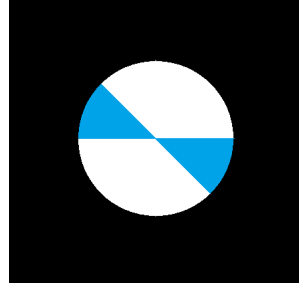


Figure 5-1: Rotating Phase PD: The black locations are outside the aperture so the amplitude is zero. The white and blue is inside the aperture so the amplitude is one. At the blue wedges a phase θ is added to the incoming wavefront.

using the rotating amplitude mask, the creators were able to reconstruct details in the image that they could not retrieve without it. When using the proposed rotating PD similar shapes of PSFs are created as when using the amplitude mask from literature. Those can be seen in Figure 5-2. Depending on the amount of phase θ in the phase diversity, the Optical Transfer Function (OTF) also obtains similar shapes.

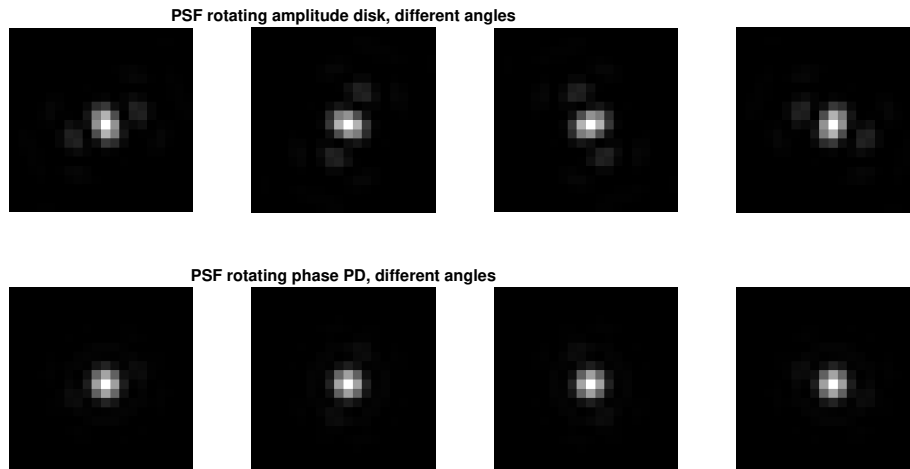


Figure 5-2: PSFs of the rotating amplitude disk from literature and the proposed rotating phase PD.

5-1-2 Rotating half phase Phase Diversity

Inspired on the proposed rotating phase PD in the previous section, the rotating half phase PD is proposed. This PD can be seen in Figure 5-3. Now at half the aperture a phase θ is added as PD. This PD is rotated 90 degrees from one image to another.

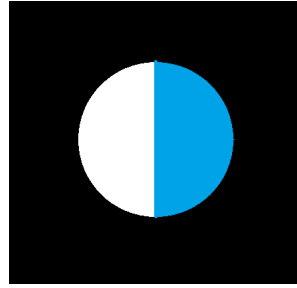


Figure 5-3: Rotating half phase PD: The black locations are outside the aperture so the amplitude is zero. The white and blue is inside the aperture, the amplitude is one. At the blue half of the aperture a phase θ is added to the incoming wavefront.

5-1-3 Spiral Phase Diversity with TIP

In section 4-2-2 a spiral phase mask was shown, previously it was used in combination with a modified version of the Gergberg Saxton algorithm. They used 2 images, one with the spiral mask and one without. In this thesis we will test the spiral phase mask in combination with the TIP algorithm. The applied spiral phase masks for the 4 different images is shown in Figure 5-4, for every image the phase diversity is rotated 90 degrees.

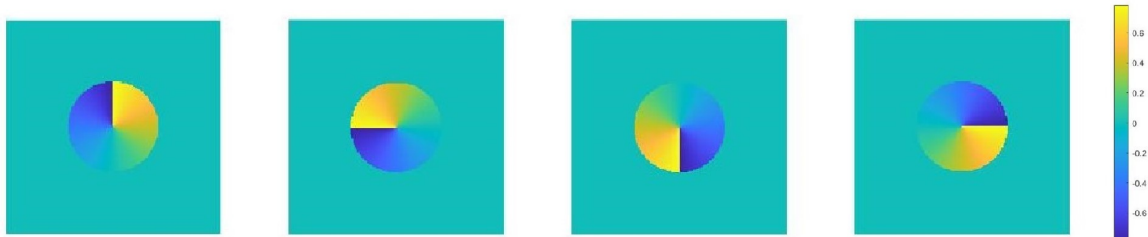


Figure 5-4: Phase of the spiral phase mask applied to four images.

5-2 Optimization based phase diversities

As mentioned in section 2-2, if the frequency spectrum of the PSF, the OTF, goes to zero or decreases a lot, it will also not be represented in the image so you will not be able to retrieve it, or when there is noise present this will be enlarged. In this section we try to find a PD that leads to a combination of MTFs that do not all decrease at the same frequencies. The equation for the MTFs for the N phase diversities is given in Equation 5-1.

$$|H_n| = |\mathcal{F}\{h_n\}| = |\mathcal{F}\{|\mathcal{F}\{A^{i(\phi+\theta_n)}\}|^2\}| \quad n = 1..N$$

$$\theta = \sum_i \alpha_i Z_i \quad (5-1)$$

Here n denotes the n^{th} diversity image. In this section we will work with $N = 4$ diversity images. The Point Spread Function (PSF) corresponding to the pupil function $Ae^{i(\phi+\theta_n)}$,

is called h_n . The PD θ will be expressed in terms of Zernike polynomials, as explained in section 2-1-1. Z_i denotes the i^{th} Zernike Polynomial and α_i its amplitude.

To generate this replacement of the decreased frequencies, in the following sections we try to find a PD that leads to MTFs that are "as different as possible" in terms of different metrics. Those metrics are the Peak Signal to Noise Ratio (PSNR) in Equation 3-14, Structural Similarity (SSIM) from Equation 3-15 and the metric proposed by Miyamura from Equation 4-2. These optimizations are performed without any knowledge on the aberrations, so in the optimization we put the aberration ϕ to zero.

5-2-1 Optimizing Modulation Transfer Functions in terms of PSNR

In the first optimization, four phase diversities are searched to apply to four images. We try to obtain phase diversities θ that have MTFs as different as possible in terms of PSNR, when there is no unknown aberration ϕ present ($\phi = 0$). So the cost function M in Equation 5-2 is minimized over the Zernike polynomials in the phase diversity θ in Equation 5-1. The 4th till 15th Zernike polynomial are used. The amplitude of those Zernike polynomials α_i $i = 4 \dots 15$ is the decision variable.

$$M = \text{psnr}(|H_1|, |H_2|) + \text{psnr}(|H_1|, |H_3|) + \text{psnr}(|H_1|, |H_4|) \dots \quad (5-2)$$

$$\dots + \text{psnr}(|H_2|, |H_3|) + \text{psnr}(|H_2|, |H_4|) + \text{psnr}(|H_3|, |H_4|)$$

The function for the PSNR can be found in subsection 3-4-1. The equation for the MTF $|H|$ is given in Equation 5-1. To minimize this cost function a multistart alterior point algorithm is used in MatLab, a bound was defined for the amplitude α_i of the Zernike Polynomials.

The four phase diversities coming from this optimization are shown in the bottom row of Figure 5-5. The size of the phases in this PD is large, so it is wrapped in the image from $-\pi$ to π . The large amount of phase diversity deteriorates the images too much to improve the

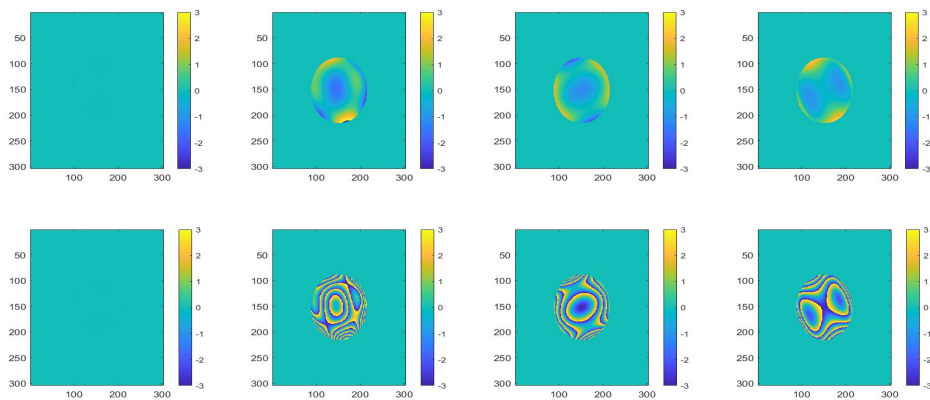


Figure 5-5: The phase diversity shapes obtained by minimizing the PSNR are shown in the bottom row, the scaled and used version of the phase is shown in the top row.

reconstructions, compared to images without this diversity. Therefore the amplitude of the

PD is scaled, so the largest Root Mean Square (RMS) error of these four phase diversities, is equal to the maximum RMS error of the Defocus PD it is compared to. The scaled, used versions are shown in the top row of Figure 5-5. These we call the Optimized PSNR PD. In the simulations described in section 5-3, we test whether they improve the reconstruction compared to Defocus PD.

5-2-2 Optimizing Modulation Transfer Functions in terms of SSIM

Here the same procedure is used to obtain the PD as in the previous section. This time the used metric is the SSIM. So the cost function to minimize this time is given in Equation 5-3.

$$M = \text{ssim}(|H_1|, |H_2|) + \text{ssim}(|H_1|, |H_3|) + \text{ssim}(|H_1|, |H_4|) \dots \quad (5-3)$$

$$\dots + \text{ssim}(|H_2|, |H_3|) + \text{ssim}(|H_2|, |H_4|) + \text{ssim}(|H_3|, |H_4|)$$

The function for the SSIM can be found in subsection 3-4-2. The equation for the MTFs $|H|$ can be found in Equation 5-1. The decision variable is again the amplitude of the Zernike polynomials α_i $i = 4 \dots 15$.

To minimize this metric again a multistart interior point algorithm is used in **MatLab** and the same bound was defined for the amplitude of the Zernike Polynomials a_i . The phase diversities that came from this optimization can be seen in the bottom row of Figure 5-6. The phases are scaled in the same way as subsection 5-2-1. The scaled, used version is shown in the top row. This we call the Optimized SSIM PD. This PD will also be tested with the simulations explained in section 5-3.

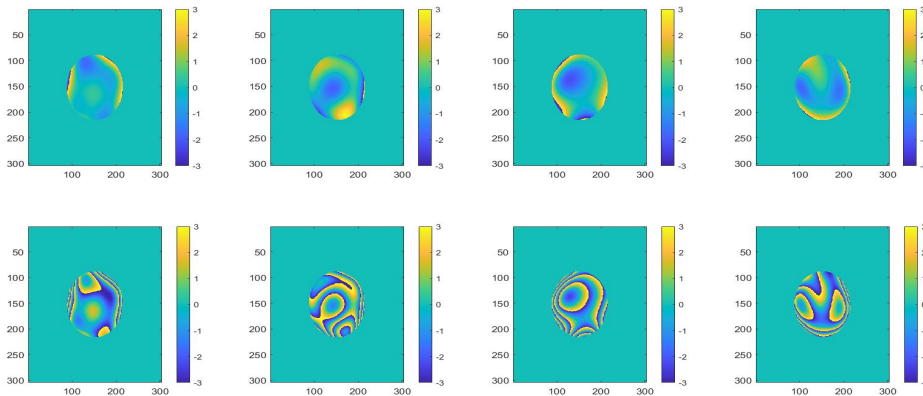


Figure 5-6: The phase diversity shapes obtained by minimizing the SSIM are shown in the bottom row, a version with fewer a scaled down version of the phase is shown in the top row.

5-2-3 Optimizing Modulation Transfer Functions in terms of Miyamura's metric.

In this optimization, again four phase diversities are searched to apply to four images. The metric used this time is the metric from Miyamura in Equation 4-2, otherwise the procedure is equal to the one performed in subsection 5-2-1.. The cost function M is given in Equation 5-4.

$$M = \sum_u \sum_v \left| \frac{|H_1|^2 - |H_2|^2}{|H_1|^2 + |H_2|^2} + \frac{|H_1|^2 - |H_3|^2}{|H_1|^2 + |H_3|^2} + \frac{|H_1|^2 - |H_4|^2}{|H_1|^2 + |H_4|^2} \dots \right. \quad (5-4)$$

$$\left. \dots + \frac{|H_3|^2 - |H_2|^2}{|H_3|^2 + |H_2|^2} \frac{|H_4|^2 - |H_2|^2}{|H_4|^2 + |H_2|^2} + \frac{|H_3|^2 - |H_4|^2}{|H_3|^2 + |H_4|^2} \right|$$

The equation for the MTFs $|H|$ can be found in Equation 5-1. The decision variable is again the amplitude of the Zernike polynomials α_i $i = 4 \dots 15$. To maximize this metric a multistart alterior point algorithm is used in `MatLab`, a bound was defined for the amplitude of the Zernike Polynomials α_i . The phase diversity that came from this optimization can be seen in the bottom row of Figure 5-7. Again the phases are quite large so they will be scaled again equally to the previous sections. The scaled, used version is shown in the top row. We call this the Optimized Miyamura PD.

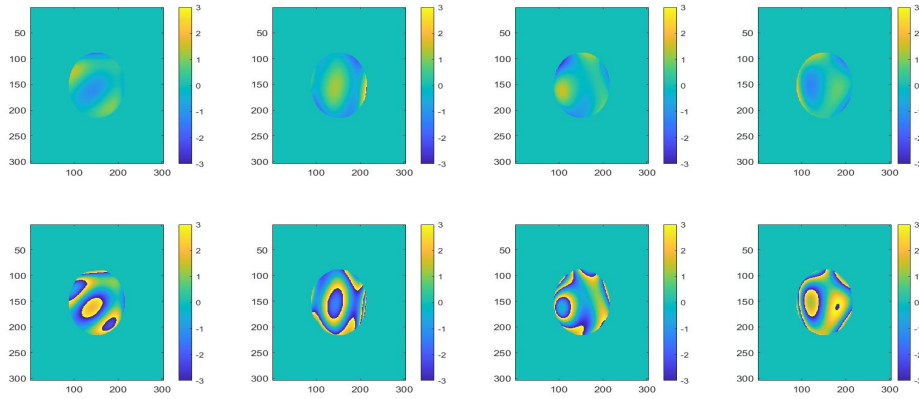


Figure 5-7: The phase diversities obtained by minimizing the Metric from Miyamura are shown in the bottom row, the scaled and used version of the phase is shown in the top row.

5-3 Simulations

To test the effect of the different proposed Phase Diversities, simulations are performed. In the simulations the formation and deterioration of images is simulated for several objects, with different incoming wavefront and noise characteristics. The simulated objects can be seen in Figure 5-8. For each combination of characteristics and objects, at least 10 simulations are performed. The parameters that are changed can be found in Table 5-1. The reconstructions that were made with TIP are compared to the ground truth of the image because in these simulations this is known. This comparison is done in terms of PSNR and SSIM. These metrics are discussed in section 3-4. When experiments would be performed, a different metric has to be chosen, for example the one used in section 4-2-1.

In the following section some examples will be given to illustrate the results and the results will be discussed. In this discussion we will compare the results of the proposed PDs to not

parameter	inputs
object	object 1: Tiger object 2: Cow object 3: Giraffe
incoming wavefront	Zernike Polynomial based lower order wavefront Kolmogorov phasescreens Sparse
RMS wavefront error	0.2 0.4 0.6 0.8 1.0 1.2 1.4
standard deviation additive gaussian noise or SNR poisson noise	0 20 dB 0.001 28 dB 0.005 36 dB 0.01 44 dB 0.02 52 dB

Table 5-1: Parameters used in simulations, the objects can be found in Figure 5-8.

using PD, to using Defocus PD and in some cases an existing diversity method. Those are all simulated in the same manner.

5-4 Results of the simulations

In this section we will discuss the results of the simulations for the different wavefronts and types of noise. We will compare the proposed PDs to Defocus PD or using no PD at all. In discussing the results some visual examples of reconstruction will be used and some plots of the PSNR and SSIM metric for the reconstructed object. For more data regarding the results, contact the author.

The results of the lower order and Kolmogorov wavefronts were quite similar and will be discussed in the upcoming sections. For the simulated sparse wavefronts the mean results in terms of PSNR and SSIM are similar as well. However the standard deviation of the results is very large, especially when the Peak to Valley wavefront error gets closer to $\pm\pi$. Figure 5-9 shows this for a Peak to Valley wavefront error of $-4/7\pi$. An explanation for these standard deviations for sparse wavefronts can be, that the characteristics of the different used sparse wavefronts are very different and deteriorate the images in largely varying amounts. Because of these high deviations, the results coming from the sparse wavefronts will not be discussed in the following sections.

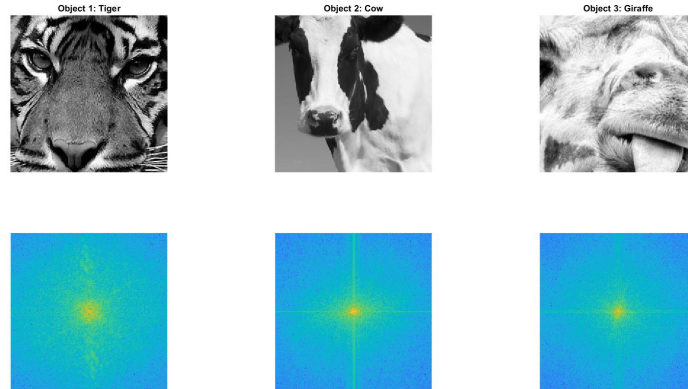


Figure 5-8: The three objects used in simulations in the top row and the absolute value the corresponding Fourier transforms in the bottom row.

5-4-1 Rotating phase and rotating half phase

First we will discuss the results of the used rotating phase PD and rotating half phase PD explained in section 5-1. Because they are inspired on the rotating amplitude disk in section 4-2-1, this amplitude diversity was also simulated to be able to compare the performance of the new phase diversities to the original amplitude diversity. For all parameter combinations from Table 5-1 at least 10 simulations have been performed.

The results of the object reconstructions with Kolmogorov phase screens and the lower order wavefronts are quite similar when there is Gaussian noise present in terms of PSNR and SSIM. The mean PSNR and SSIM of the object reconstructions in the simulations are plotted in Figure 5-10 for lower order wavefronts. In Figure 5-11 these results are displayed for Kolmogorov phase screens.

Comparing the PSNR for Gaussian noise

The highest PSNR is achieved using Defocus PD when there is Gaussian noise in the images. For all parameters in Table 5-1, Defocus PD outperforms the other phase and amplitude diversities in this section, except when there is no noise present. In practice having zero noise is not a realistic situation. When comparing the proposed rotating phase, rotating half phase and amplitude diversity, in terms of PSNR the amplitude diversity outperforms the PDs for lower additive Gaussian noise. When the additive Gaussian noise gets big, the rotating half phase starts to achieve the same PSNR as the amplitude diversity.

Comparing the SSIM with gaussian noise

When a high RMS wavefront error is present, the differences between the different simulations are very small in terms of SSIM. At lower RMS wavefront errors, Defocus PD gets outperformed by the rotating amplitude and phase diversities except for the second object. This

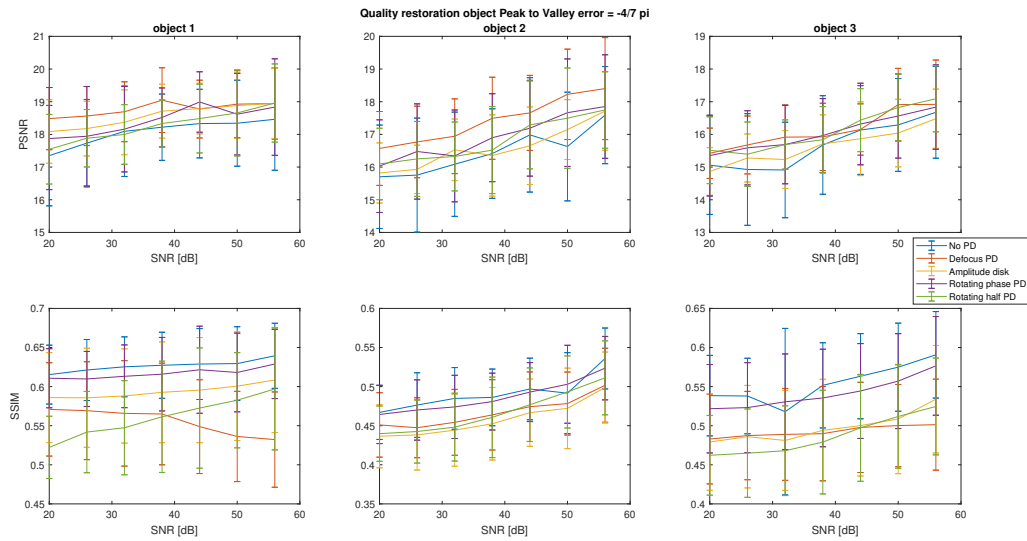


Figure 5-9: Quality object reconstructions for the rotating phase PD and rotating half PD, for poisson noise and sparse wavefronts with a Peak to Valley wavefront error of $-4/7 \pi$. The quality is measured in PSNR and SSIM of the reconstruction of the object. The mean is given by the line and the error bars denote the standard deviation. When sparse wavefronts are used, the standard deviation of the results is very high.

might be because the second object consists of large areas, and less small details, therefore still having some defocus in a reconstruction might influence it less.

Poisson Noise

When Poisson noise is present the results are different. In Figure 5-12 we see the PSNR and SSIM for different SNRs when the RMS wavefront error is 1. In the top row the results are shown for the PSNR metric, the rotating phase PD and rotating half PD performs best. From the results for the SSIM metric, we can conclude that using no PD or the rotating phase PD perform best. Only if the RMS wavefront error becomes very small, the Defocus PD performs better.

The fact that the rotating phase PD and rotating half PD outperform the rotating amplitude disk when Poisson noise is present can be explained by the fact that the Signal to Noise Ratio (SNR) for the amplitude diversity decreases because part of the light is blocked. A visual example is shown in Figure 5-13. This example shows the object and an aberrated image without PD applied. An image without the Poisson noise shows the effect of it. In this example object reconstruction using no PD, Defocus PD and the PDs based on literature are given.

5-4-2 Spiral Phase Diversity

The performance in terms of PSNR and SSIM of both the spiral and rotating phase PD is shown in Figure 5-14 for Poisson noise and lower order wavefronts with a RMS wavefront

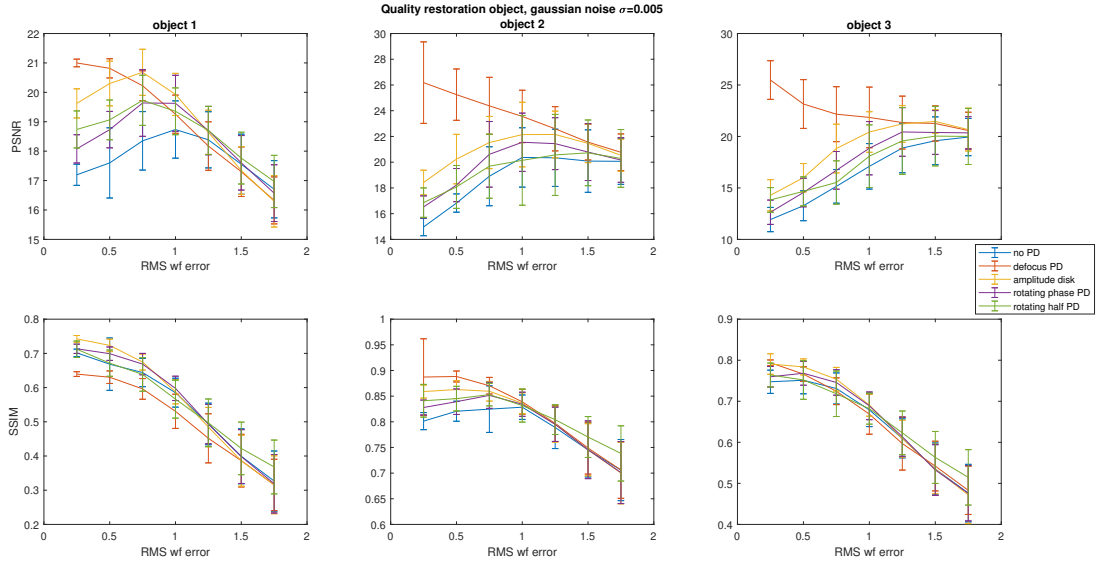


Figure 5-10: Quality object reconstructions for the rotating phase PD and rotating half phase PD, for lower order wavefronts with Gaussian noise $\sigma = 0.005$. From 30 simulations the mean and standard deviation of the PSNR and SSIM are displayed. For comparison the result of using no PD and the amplitude disk it was inspired on are also given.

error of 1. For both metrics the result of the Spiral PD is similar to the rotating phase PD. An example of a restoration with Poisson noise is given in Figure 5-13.

When the images contain Gaussian noise, again for both metrics the results are similar. Except when the standard deviation of the Gaussian noise becomes $\sigma = 0.02$ the spiral PD outperforms the rotating phase PD.

5-4-3 Optimized Phase Diversities

In this section we will compare the three optimized diversities to using Defocus PD and using no PD. The three diversities are the PSNR optimized, the SSIM optimized and the Miyamura optimized. First we discuss the results when there is Gaussian noise and continue with the ones including Poisson noise.

Optimized PDs with Gaussian noise

When Gaussian noise is present, for the PSNR metric the Miyamura optimized PD performs better than the PSNR and SSIM optimized PDs. For the SSIM metric the three optimized PDs perform quite similar. This can be seen in Figure 5-15. The Defocus PD achieves better results in terms of the PSNR metric but not in terms of the SSIM. This is equal to the results with Gaussian noise in the previous section.

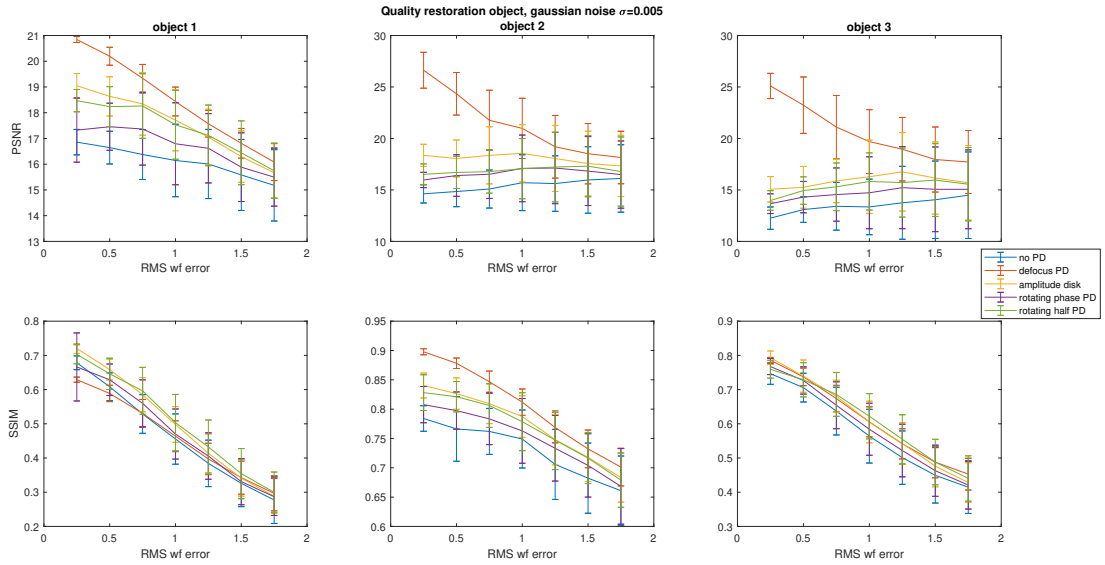


Figure 5-11: Quality object reconstructions for the rotating phase PD and rotating half phase PD, for Kolmogorov phase screens with Gaussian noise $\sigma = 0.005$. From 30 simulations the mean and standard deviation of the PSNR and SSIM is displayed. For comparison the result of using no PD and the amplitude disk it was inspired on are also given.

Optimized PDs with Poisson noise

When Poisson noise is present, the results of the PSNR metric in Figure 5-16 show, the Miyamura optimized PD outperforms the others in most cases. The result for the SSIM when poisson noise is present shows, using no PD performs best and the PSNR optimized PD performs second. Both in terms of PSNR and SSIM the miyamura optimized PD outperforms Defocus PD.

5-4-4 Conclusions on the proposed predefined Phase diversities.

In this chapter new Phase Diversity shapes were proposed. From the proposed PDs that were inspired on literature, in certain circumstances the rotating phase PD performed very good and it others the rotating half PD. The rotating phase and rotating half are quite similar. They only have a different angle of the aperture where they add phase to the unknown wavefront, respectively 45 and 180 degrees. Future research could look into the optimal angle of the wedges in the PD in Figure 5-1 and the optimal amplitude of this phase. For future research the optimal angle of rotation could be interesting. The spiral PD performed similar to the rotating phase PD.

From the proposed Phase Diversity shapes based on optimizing the MTF, the best results were obtained using the Miyamura optimized PD. When Gaussian noise was present this PD performed equally good or better than the others for both the PSNR metric and the SSIM metric. When Poisson noise was present the Miyamura optimized PD performed better in terms of PSNR. The results of the SSIM metric were better for the PSNR optimized PD

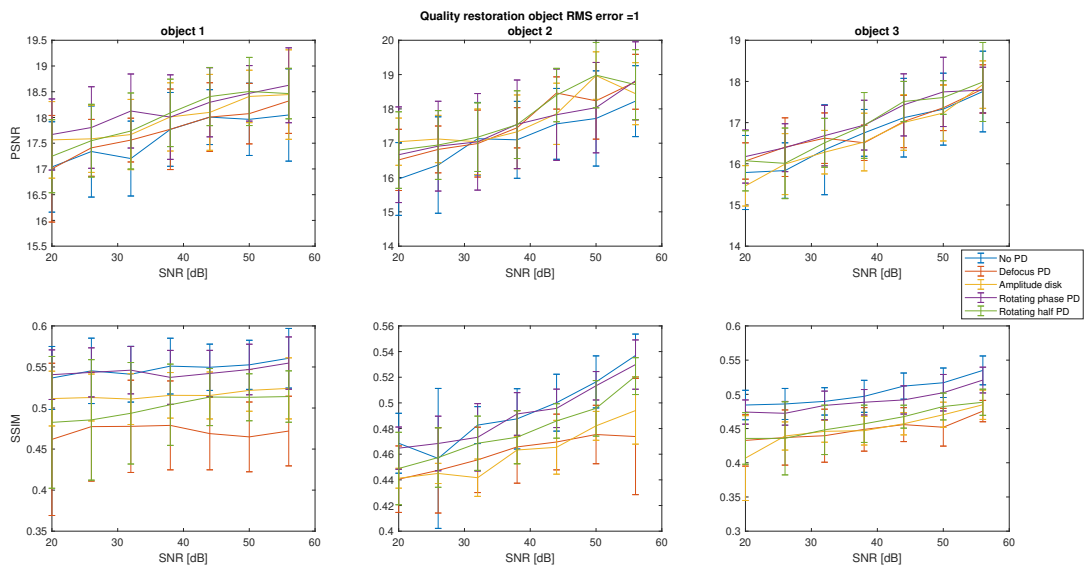


Figure 5-12: Quality object reconstructions for the rotating phase PD and rotating half PD, for poisson noise and lower order wavefronts with a RMS wavefront error of 1. The quality is measured in PSNR and SSIM of the reconstruction of the object. The mean is given by the line and the error bars denote the standard deviation. The results in terms of PSNR in the top row, show the rotating phase PD and rotating half PD both outperform using no PD, Defocus PD or the rotating amplitude disk. From the SSIM metric, we conclude that using no PD and the rotating phase PD perform best.

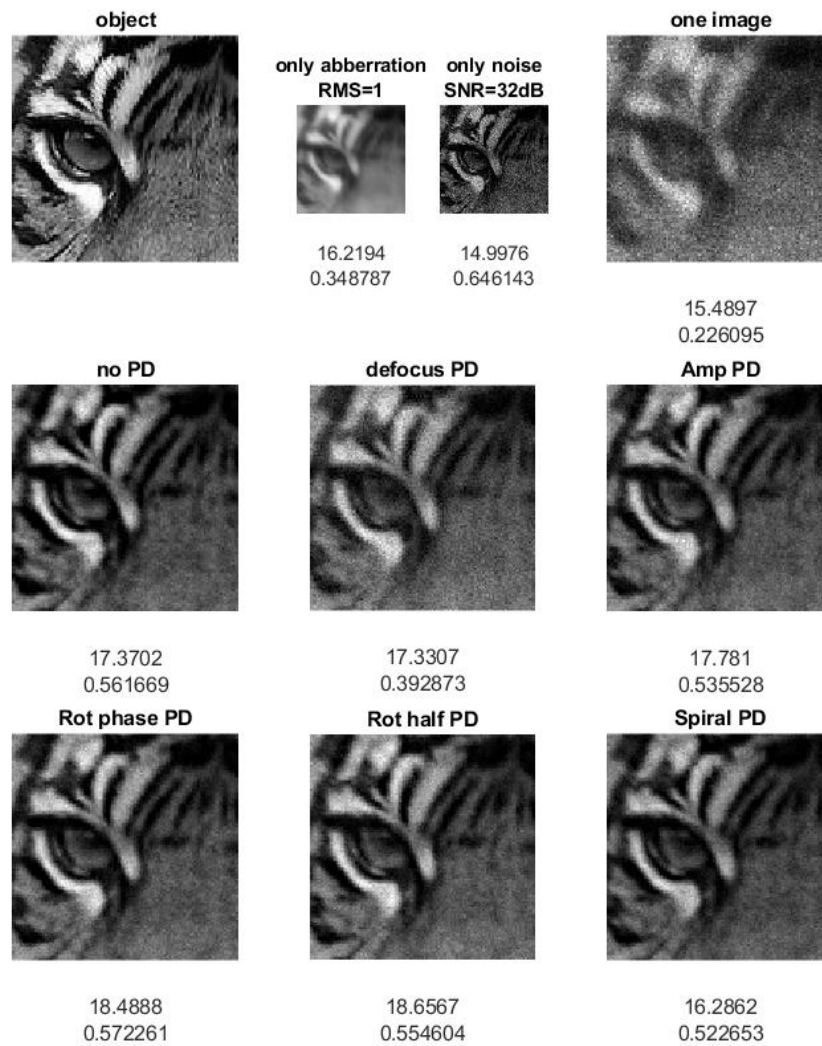


Figure 5-13: Example of reconstructions with different diversities with Poisson noise present. In the top row we see the object, an image where only the aberrated wavefront is present and the noise is not yet added. The wavefront is a lower order wavefront with RMS=1. Besides that we see an image where only the poisson noise is added. In the top right we see one of the images without PD added. In the second and third row we see the different reconstructions with their PSNR and SSIM. The rotating half PD leads to the highest PSNR and the rotating phase PD leads to the highest SSIM.

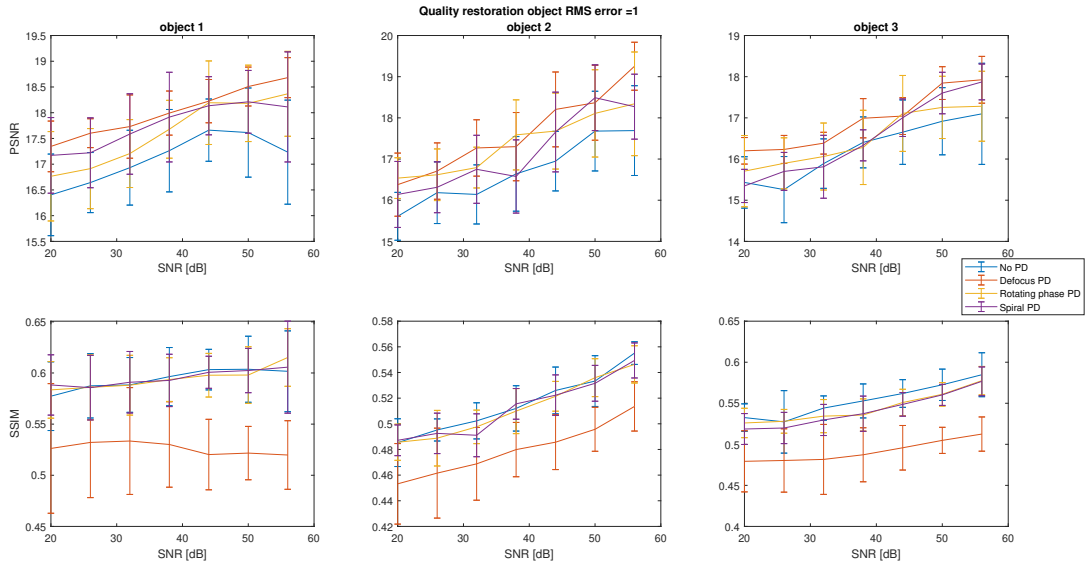


Figure 5-14: The mean and standard deviation of the PSNR and SSIM of the reconstructions for a lower order wavefront, the RMS wavefront error is 1 and the objects and wavefront errors from Table 5-1. The mean is given by the line and the errorbars denote the standard deviation. Here we compare the rotating spiral PD to the rotating phase PD

when Poisson noise was present.

When there is gaussian noise present, the rotating phase/ rotating half and the Miyamura optimized PD, all outperformed Defocus PD in terms of SSIM. In terms of SSIM, when the Gaussian noise is low to medium, the Miyamura optimized PD performed best. If the Gaussian noise became higher, the rotating half PD performed best. To maximize the PSNR, Defocus PD should be used. In terms of PSNR the results of the Miyamura optimized PD outperforms the rotating phase and rotating half.

When Poisson noise is present, these three PDs outperform Defocus PD in terms of PSNR and SSIM. For lower RMS wavefront errors, the Miyamura PD produces a higher PSNR and the rotating phase PD produces a higher SSIM. For higher RMS wavefront errors, the rotating phase PD performs better both in terms of PSNR as SSIM. However for the higher RMS wavefront errors, using no PD at all performs best in combination with Poisson noise.

To validate the results from the simulation, the rotating phase PD and Miyamura optimized PD can be tested empirically in future research.

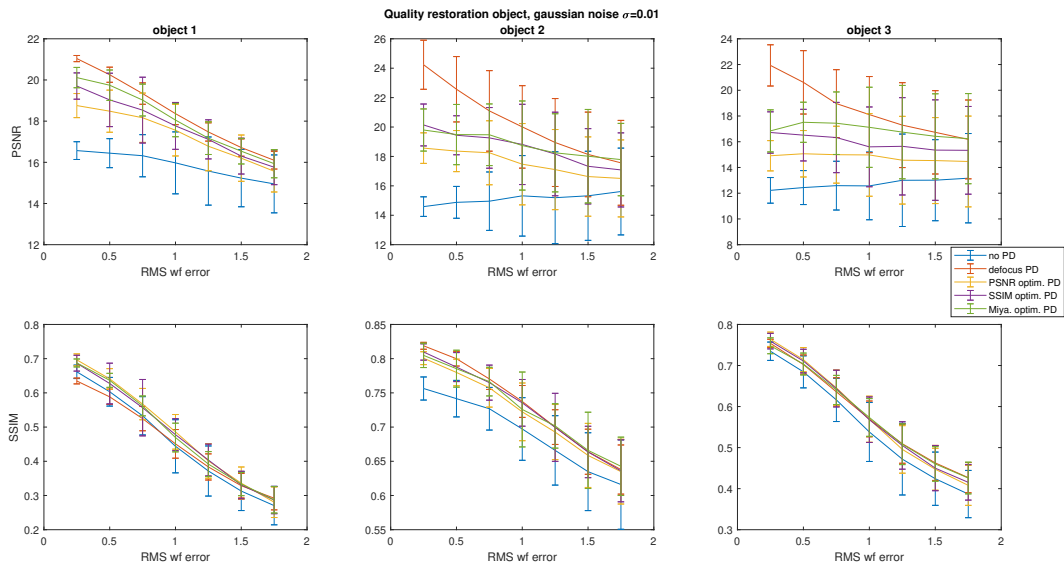


Figure 5-15: The mean and standard deviation of the PSNR and SSIM of the reconstructions for a Kolmogorov wavefront, the Gaussian noise has $\sigma = 0.01$ and the objects and wavefront errors from Table 5-1. The mean is given by the line and the errorbars denote the standard deviation.

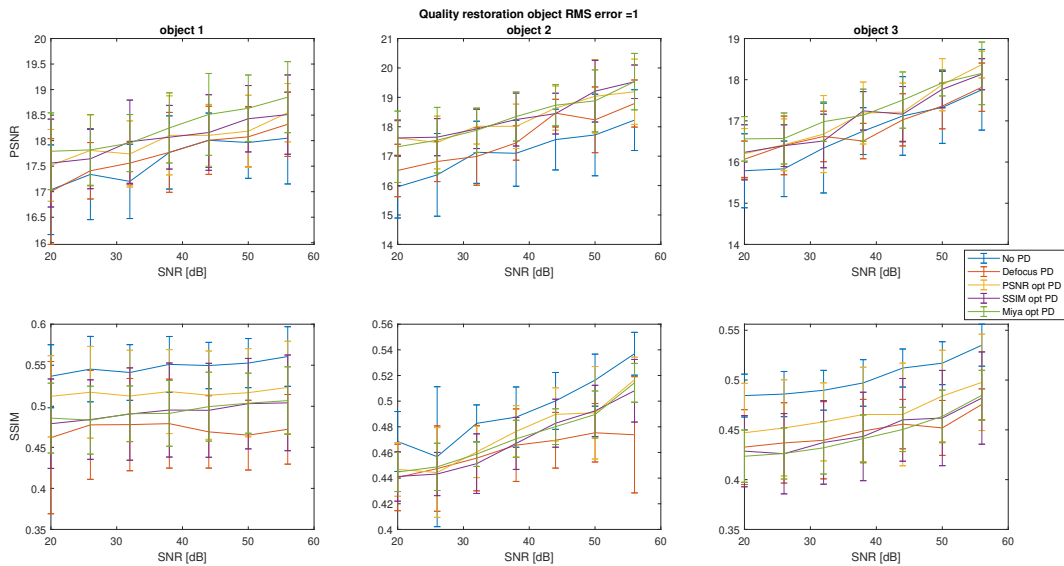


Figure 5-16: The mean and standard deviation of the PSNR and SSIM of the reconstructions for Poisson noise and lower order wavefronts with RMS wavefront error 1. The mean is given by the line and the errorbars denote the standard deviation. The results of the PSNR metric show the Miyamura optimized PD performs best. The results of the SSIM metric show the PSNR optimized PD performs best except for using no PD at all.

Phase Diversity Dependent on Previous Images

In this chapter we will look into the second case, the case where we already have N images and search for the Phase Diversity (PD) θ to add at the aperture for the next image so we can improve the reconstruction of the original object. Like we did in the previous chapter where we predefined the PD, we again want to design our PD such that the low values in the frequency spectra of the N images are moved to a different location. Because as mentioned before, if the Optical Transfer Function (OTF) goes to zero at a certain frequency, this frequency will also not be represented in the image. Therefore it will not be possible to retrieve the information at that frequency, or when there is noise present it can blow up. The equation leading to this blowing up of the noise can be Equation 6-1

$$I = H \circ O + N \quad O = \frac{I + N}{H} = \frac{0 + N}{0} \quad (6-1)$$

Therefore we will first design a weighting mask that shows where the decreased frequencies of the images are. Next we design a PD that makes sure those frequencies are not decreased in the $N + 1^{th}$ image.

6-1 Finding the decreased frequencies.

In Figure 6-2 a) to f) a visual example is shown of how the decreased frequencies are found. First we calculate the absolute value of the frequency spectra of all N images taken so far, as in Equation 6-2. For the N images in Figure 6-2 a) these frequency spectra are displayed below the corresponding images.

$$|I_n(u, v)| = |\mathcal{F}\{i_n(x, y)\}| \quad \text{for } n = 1 \dots N \quad (6-2)$$

We are interested in the frequencies that are decreased in all images, because they are the ones that cannot be retrieved from the N images for the object reconstruction. To see which

frequencies are not represented or very small in any of the N images, we take the maximum value of the Fourier transform of the images at each frequency point (u, v) . This is represented in Figure 6-2 c) and Equation 6-3.

$$I_{max}(u, v) = \max_n |I_n(u, v)| \quad (6-3)$$

Since we want to increase the frequencies that were decreased in the N images, we take the inverse of this maximum in 6-2 d) as a weighting mask W . Now a higher value in W for a certain frequency means a value that frequency was less represented in the images. A few adjustments are made to the weighting mask: first we remove the high frequencies (Figure 6-2 e.) and second apodization is added with a Gaussian filter(6-2 f.). Both steps are taken because these lower frequencies are considered very important to be captured. An example to illustrate this can be seen in Figure 6-1. The third adaptation of the weighting mask is that all values below 1 are set to 0. This is done because the Modulation Transfer Function (MTF) is large at these frequencies and does not need a boost. The weighting mask W is given as an equation in 6-4.

$$W(u, v) = \begin{cases} w_g(u, v) \cdot \frac{1}{I_{max}(u, v)} & \forall u^2 + v^2 < f_{cut} \\ 0 & \forall u^2 + v^2 > f_{cut} \end{cases} \quad (6-4)$$

if $W(u, v) < 1 \rightarrow W(u, v) = 0$

In this equation w_g is the Gaussian apodization filter, f_{cut} the frequency above which we say the frequencies are not important to reconstruct. Now the higher values in our weighting mask W are the frequency we most want to be present in the MTF of our $N + 1^{th}$ image.

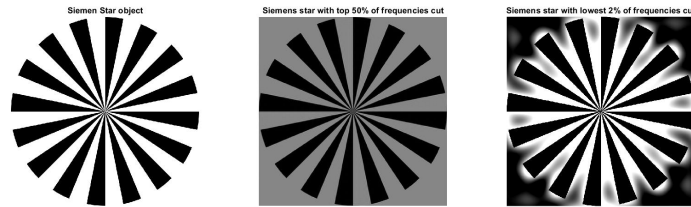


Figure 6-1: On the left the Siemens star, in the middle a variation where the highest 50% of the frequencies have been removed and on the right a version where the lowest 2% of the frequencies have been removed.

6-2 Designing the Phase Diversity

To design the PD, we want the values of the MTF corresponding to the PD to be highest at the frequencies with the higher values in the weighing mask W . To achieve this the metric

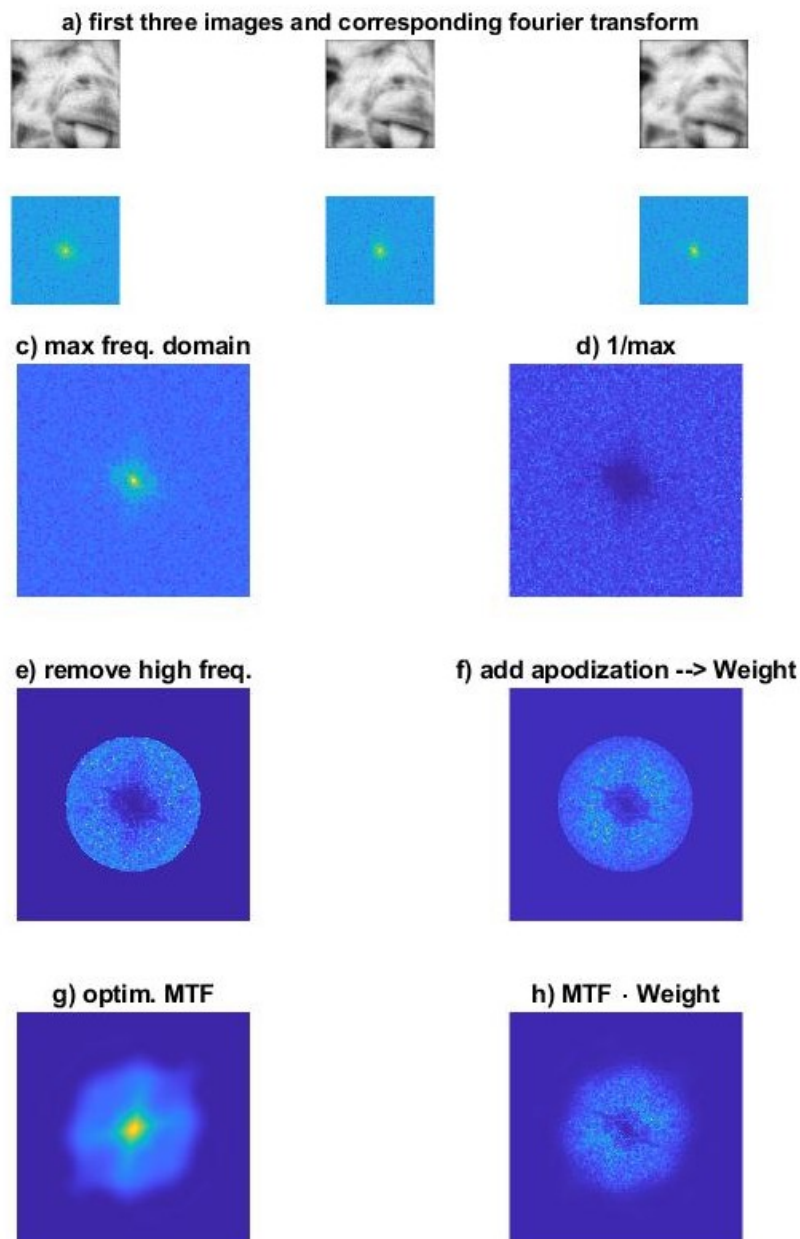


Figure 6-2: An example method used to determine the PD that will be added to the $N + 1^{th}$ image. a) The top row shows the $N (=3)$ images that have been taken. On these images Defocus PD was already applied. The absolute value of the corresponding frequency spectra is calculated and displayed in the second row on logarithmic scale. In image c.) $\max(\text{MTF})$, at each frequency point the maximum value of the N frequency spectra is taken as in Equation 6-3. In image d.) at each frequency point we divide 1 by maximum value. Next in e.) the high frequencies are removed and in f. apodization is added. Now all points less than 1, are set to zero. This is now our weighting mask W for the optimization as in Equation 6-4. In the optimization we try to find a new MTF (in this case g.) that when it is pointwise multiplied by the mask f.), as can be seen in h.) the sum over all pixels reaches the highest value.

M in Equation 6-5 is minimized over the amplitude of the Zernike polynomials a_i .

$$M = - \sum_{u,v} W(u,v) \circ |H(u,v)| = - \sum_{u,v} W(u,v) \circ \left| \mathbf{F} \left\{ \left| \mathbf{F} \left\{ A(x,y) \cdot \exp^{i\theta(x,y)} \right\} \right|^2 \right\} \right| \quad (6-5)$$

$$\theta = \sum_i a_i Z_i \quad i = 4 \dots 15$$

In which W is the weighting mask described in Equation 6-4. The weighting mask is point-wise multiplied with the MTF. The MTF is created with the simulated lens when the only aberration is the PD θ is present and the formula was previously explained in Equation 5-1. This PD θ is constructed from the 4th till 15th Zernike polynomial. The first three Zernike polynomials have been discarded because they don't change the shape of the Point Spread Function (PSF), only lower order Zernike polynomials have been used because as in the research from Smith in section 4-3 using Lower order polynomials outperformed using higher order ones. An example of the optimized MTF and the multiplied version are described in respectively Figure 6-2 g.) and h.). The metric value is calculated by summing all pixels from this multiplied version.

For the optimization a multi-start interior point algorithm is used. The decision variable $a_i, \quad i=4 \dots 15$ is bounded from 0 to 0.25 for the optimization. These bounds have been chosen, because when a larger amount of phase is added as PD, it deteriorates the image too much to get a good reconstruction from it, as was the case with the large PDs in subsection 5-2-1.

In the simulations we assume we have $N = 3$ images and we search the optimal PD for the $N + 1^{th} = 4^{th}$ image. The $N=3$ images are the same as the first three for Defocus PD case. For the 4^{th} image we add the optimized PD θ to the unknown aberration ϕ .

6-3 Results of method for defining the Phase Diversity for the N+1th image

To determine whether the method proposed for finding a PD for the N+1th image in the previous sections improves the reconstructions, simulations were performed. The simulations had the same properties as the ones in section 5-3. In the simulations we set $N = 3$ and try to find the optimal PD for the 4^{th} image. In this chapter we will discuss the results of these simulations for the different types of wavefronts and noise as given in Table 5-1.

6-3-1 Gaussian noise

When Gaussian noise is present, as was seen in the previous chapter, using Defocus PD outperforms using no PD in terms of Peak Signal to Noise Ratio (PSNR), but performs worse in terms of Structural Similarity (SSIM). In the situation of Gaussian noise the new method performs equal or better than the Defocus PD, both in terms of SSIM and PSNR. This can be seen for a lower order wavefront in Figure 6-3 and for a kolmogorov phasescreen in Figure 6-4. However in terms of SSIM the new method often still gets outperformed by using

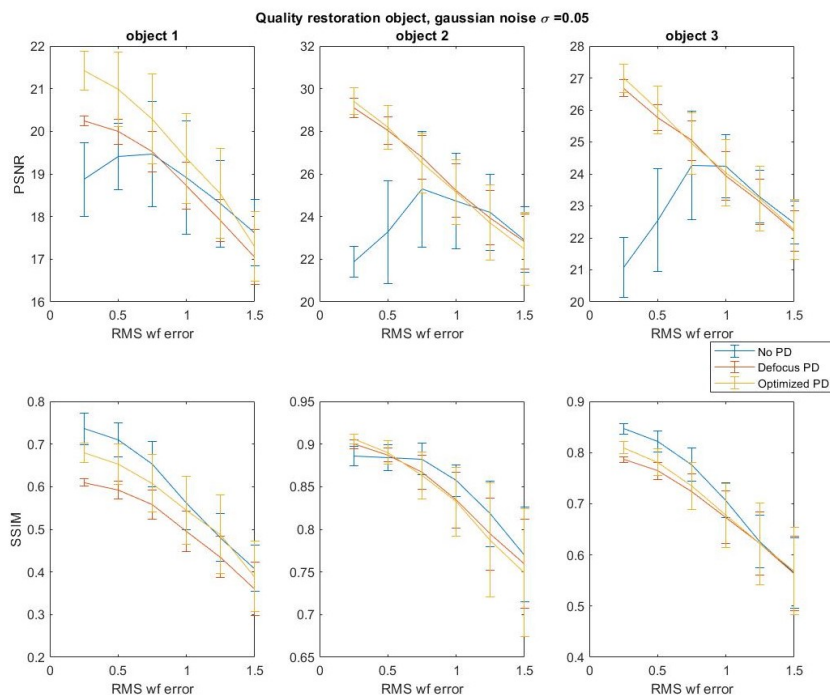


Figure 6-3: The mean and standard deviation of the PSNR and SSIM of the reconstructions for a Lower Order wavefront, gaussian noise with $\sigma = 0.005$ and the objects and wavefront errors from Table 5-1. The mean is given by the line and the errorbars denote the standard deviation.

no PD at all. The fact that it has comparable results to the Defocus PD can be explained by the fact that the first three images are equal. The author expects the method to exceed the results of Defocus PD even more, when the PD is optimized for more images ($N+2^{th}$, $N+3^{th}$).

A visual example of the reconstructions with gaussian noise can be seen in Figure 6-5. This example shows object 1: the tiger, and the restorations of it for using no PD, Defocus PD and the optimized PD. The Root Mean Square (RMS) wavefront error is 0.75 and the noise has standard deviation $\sigma = 0.005$. Below each reconstruction the PSNR and SSIM are given.

6-3-2 Poisson noise

When poisson noise is present the method does not perform well. The mean PSNR and SSIM for lower order wavefronts with a RMS wavefront error of 0.75 are given in Figure 6-6.

For a low Signal to Noise Ratio (SNR), the optimized PD method performs worse than Defocus PD and using no PD at all. When the SNR is higher the new method starts to outperform Defocus PD again, just like the Gaussian noise result. Visual examples with the same unknown wavefront error but a different amount of Poisson noise are shown in Figure 6-7 and Figure 6-8 here the SNRs are respectively 28 dB and 52 dB. These examples visually

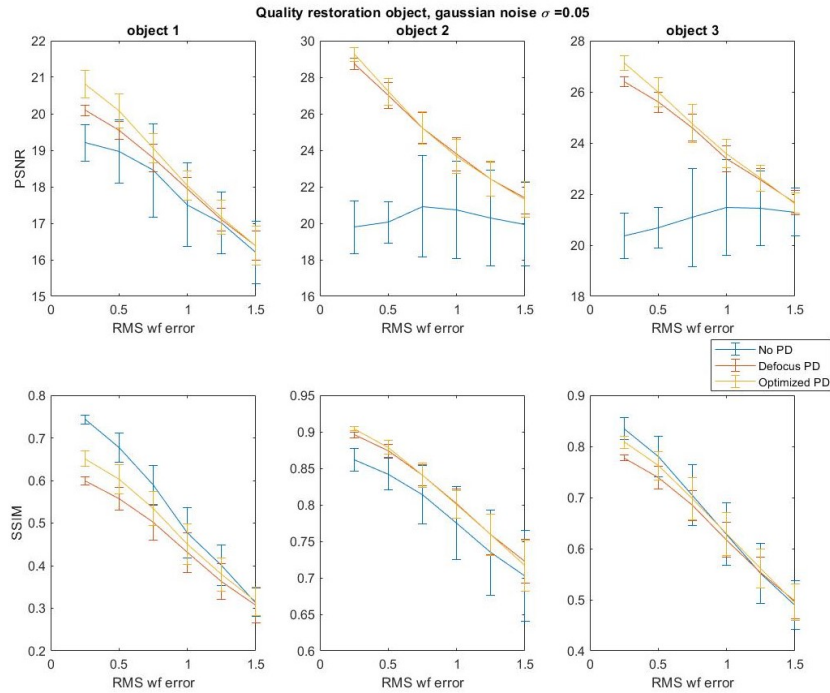


Figure 6-4: The mean and standard deviation of the PSNR and SSIM of the reconstructions for a Kolmogorov wavefront, gaussian noise with $\sigma = 0.005$ and the objects and wavefront errors from Table 5-1. The mean is given by the line and the errorbars denote the standard deviation.

show that the proposed method performs worse than Defocus PD when the SNR is low (28 dB) and better than Defocus PD when the SNR is higher (52 dB).

From the data and examples we can conclude that when the SNR is very low, it is neither good to use the new method nor to use Defocus PD. Because the poisson noise is the main distortion in the image and it is image dependent, if the image is deteriorated extra by the PD this also influences the noise. This might explain why the PD does not improve the quality of the reconstruction at lower SNRs.

6-3-3 Optimized Phase Diversities

In this section we will inspect the different phase diversities that came from the optimizations. A visual example of a created weighting mask W , the corresponding optimized MTF and PD and the object reconstruction with and without this PD are shown in Figure 6-9.

The amplitude of the Zernike polynomials for three iterations of all parameters in Table 5-1 can be seen in Figure 6-10. When there is Gaussian noise present, almost none of the PDs utilize the 7th till 10th Zernike polynomial. However when Poisson noise is present the 8th Zernike polynomial, coma, does appear in many cases. This coma is mostly added when the SNR is lower. When the SNR is low, the method also performs badly, for future research it might be interesting to see if the method performs better when the amplitude of the 8th Zernike polynomial is set to zero. The author already briefly tried this and it seemed promising.

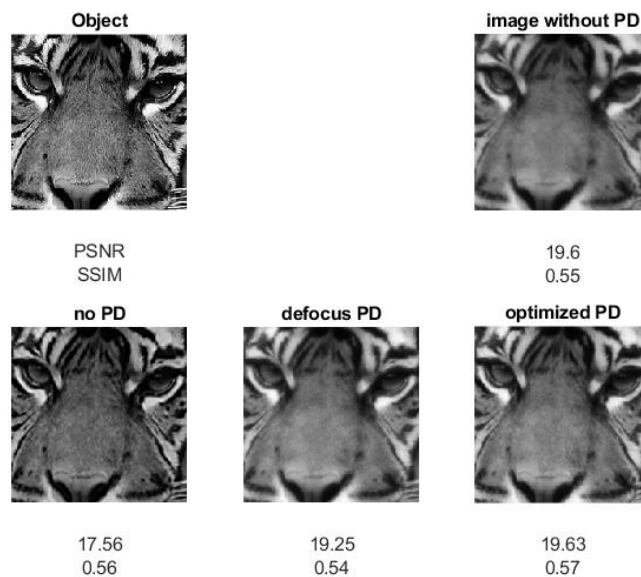


Figure 6-5: This example shows object 1: the tiger, and the restorations of it for using no PD, Defocus PD and the optimized PD. Below the restorations the PSNR and SSIM are given. Here a lower order wavefront with a RMS of 0.75 was used as the aberration and the Gaussian noise has a standard deviation of $\sigma = 0.005$.

Optimizing the PD using this method in these simulations took about 2 minutes. There are some ways to speed this up. Knowledge on the optimized PDs can be used. It might be interesting to test if leaving out the 7th till 10th Zernike polynomial leads to similar results while speeding up the optimization. Another way to improve the optimization speed is by optimizing the PD and MTF over less pixels. Than the weighting mask has to be resized as well, this will cause some information loss. However the MTFs created by the lower order Zernike polynomials, do not amplify a certain frequency but a range of frequencies, so the author does not expect this to be a problem.

6-3-4 Conclusion

Using this new method when there is Gaussian noise, in all simulated situations it performs better or as good as using Defocus PD in terms of both SSIM and PSNR. However in terms of SSIM it often still gets outperformed by using no PD at all, just like Defocus PD. The results being comparable to the Defocus PD can be explained by the fact that in the performed simulations the first three images are equal. The author expects the method to exceed the results of Defocus PD even more, when the PD is optimized for more images ($N + 2^{th}$, $N + 3^{th}$). This might be interesting for future research.

When there is Poisson noise present, at lower SNRs using the optimized PD is outperformed by using no PD at all and using Defocus PD. This could be because the poisson noise is the main distortion in the image and related to the image intensity values. If the image is deteriorated extra by the Defocus PD or optimized PD, this also influences the Poisson noise.

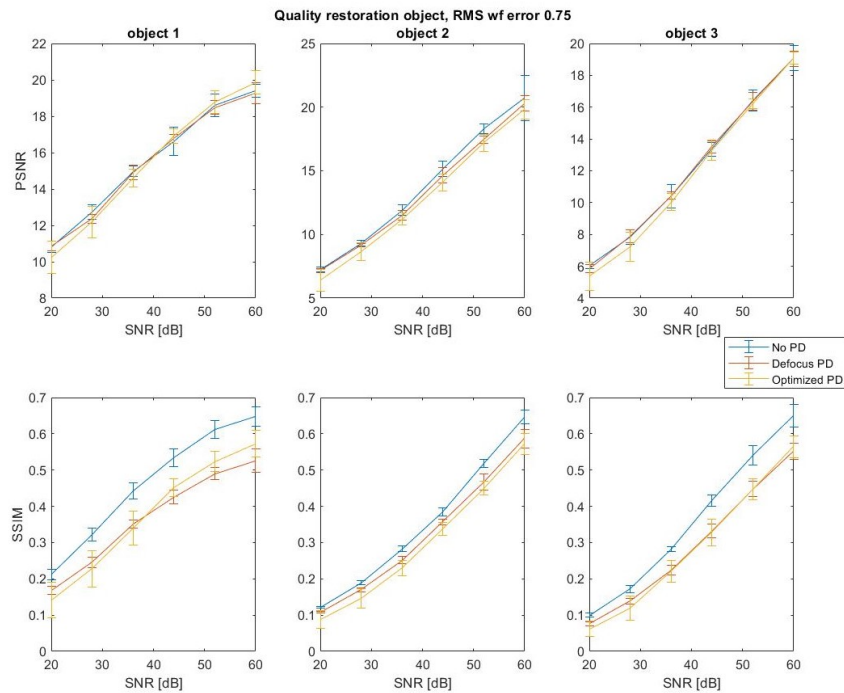


Figure 6-6: The mean and standard deviation of the PSNR and SSIM of the reconstructions for a lower order wavefront, the RMS wavefront error is 0.75 and the objects and wavefront errors from Table 5-1. From 10 iterations the mean is given by the line and the errorbars denote the standard deviation.

This might explain why the PDs do not improve the quality of the reconstruction at lower SNRs.

Another explanation could be that when the SNR is lower, the 8th Zernike polynomial (coma) often is used as part of the optimized PD, this might influence these results. This effect may be explored in future research.

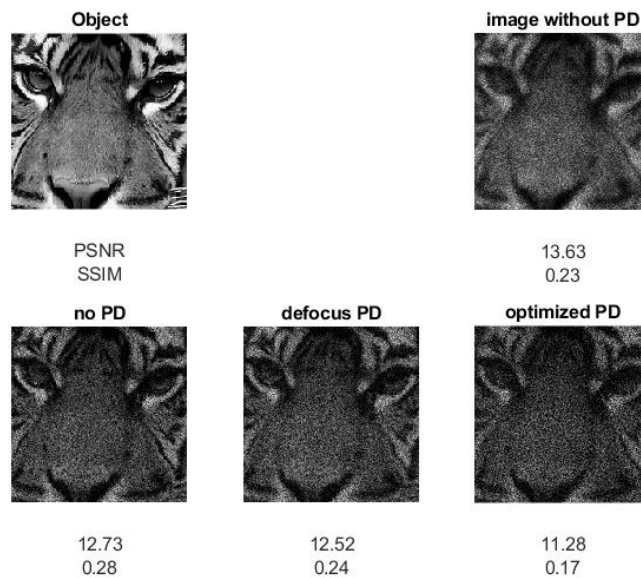


Figure 6-7: This example shows object 1: the tiger, one image without diversity applied and the restorations of it for using no PD, Defocus PD and the optimized PD. Below the restorations the PSNR and SSIM are given. Here a lower order wavefront with a RMS of 1 was used as the aberration and the Poisson noise has a SNR of 28 dB.

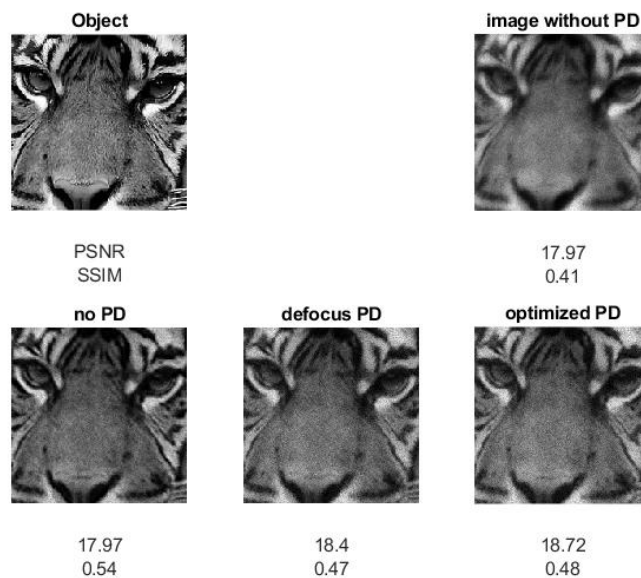


Figure 6-8: This example shows object 1: the tiger, one image without diversity applied and the restorations of it for using no PD, Defocus PD and the optimized PD. Below the restorations the PSNR and SSIM are given. Here the same lower order wavefront with a RMS of 1 was used as in Figure 6-7, this time Poisson noise has a SNR of 52 dB.

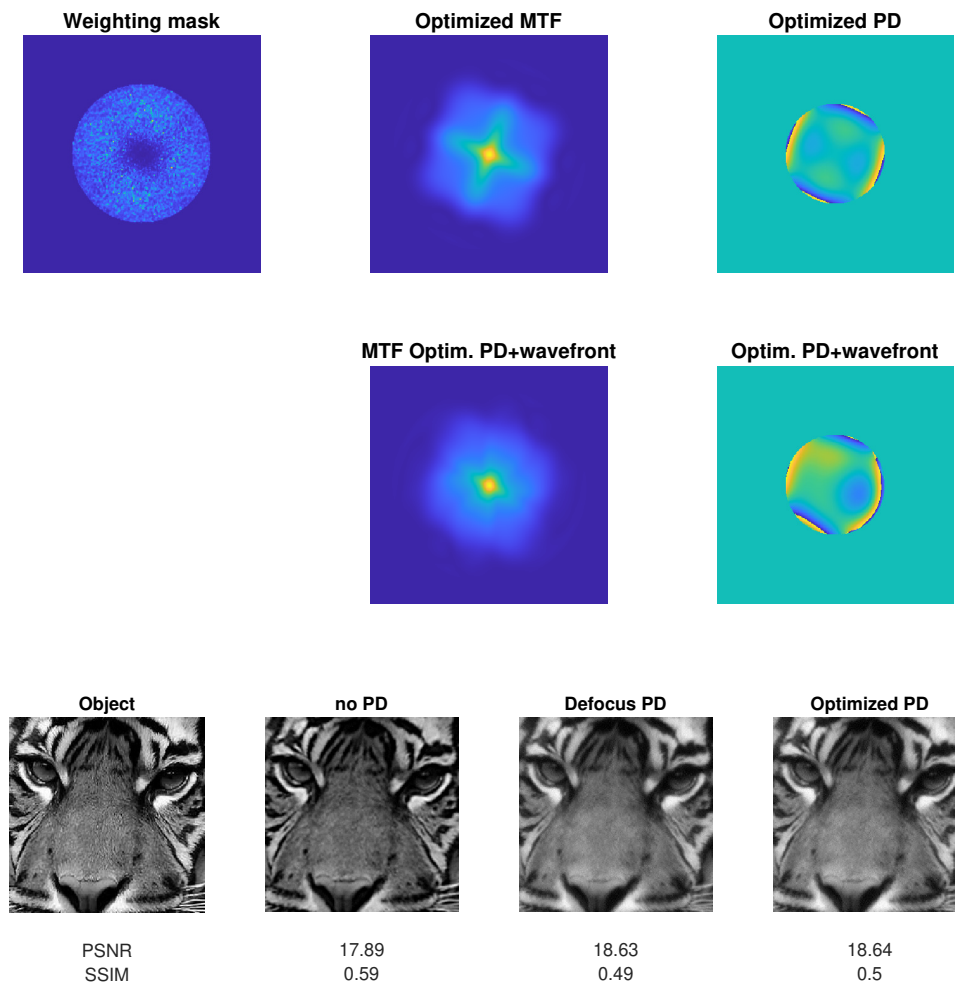


Figure 6-9: In the top row a visual example of a created weighting mask W , the corresponding optimized MTF and PD are shown. In the second row the optimized PD is added to the wavefront ϕ and the resulting MTF is given. In the bottom row object reconstructions with and without this optimized PD are shown.

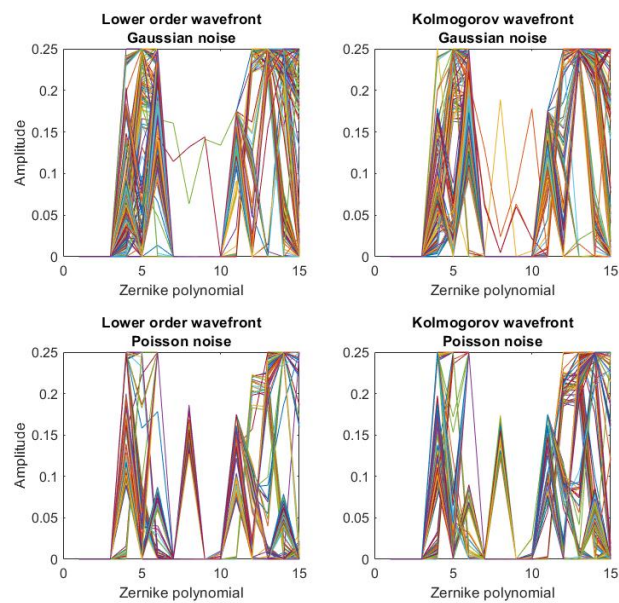


Figure 6-10: The amplitude of the Zernike polynomials in the optimized PDs for all parameters in Table 5-1. It has been split up in lower order and Kolmogorov wavefronts and in Gaussian and Poisson noise.

Conclusions and Recommendations

The goal of this thesis was to research whether there is a phase diversity that leads to a reconstruction of the object using the TIP algorithm, with a higher Peak Signal to Noise Ratio (PSNR) or Structural Similarity (SSIM) than defocus as phase diversity. Two cases are considered, first the case where no information about the object or aberrations is present and no images have been taken yet, the Phase Diversity (PD) is predefined. In the second case already some images have been taken and we look for the PD to add to the next image that improves the PSNR or SSIM as well.

In chapter 5 the first case, where the PD was predefined is researched. Several new PD shapes were proposed. Some interesting results will be highlighted here. When Gaussian noise is present from the results in terms of the PSNR metric can be concluded that Defocus PD performs best. The results in terms of the SSIM metric however are worst for the Defocus PD. The proposed Miyamura optimized PD resulted in the highest SSIM when small amounts of Gaussian noise are present. When higher amounts of Gaussian noise are present using the rotating half PD resulted in the highest SSIM.

If the images contain Poisson noise the results for using the rotating phase PD are best in terms of PSNR and SSIM. The Miyamura PD also outperforms Defocus PD. However when the Root Mean Square (RMS) wavefront error becomes larger, using no PD at all performs best when Poisson noise is present.

The rotating phase and rotating half are quite similar in shape. Future research could look into the optimal angle of the wedges in the PD in Figure 5-1 and the amount of phase that should be added there. It is also recommended to look into the optimal angle of rotation.

To validate the results from the simulation, the rotating phase PD and Miyamura optimized PD can be tested empirically in future research. Also simulating or testing these PDs with

temporal aberrations could be interesting for future research.

In chapter 6 the second case of the research question, where already some images are taken is researched. This method first locates the frequencies that are poorly presented in the already taken images. Next it optimized a PD corresponding to a Modulation Transfer Function (MTF) that enhances those frequencies. When there is Gaussian noise, the new method performs better or as good as using Defocus PD in terms of SSIM and PSNR. However in terms of SSIM it often still gets outperformed by using no PD at all. The fact that it has comparable results to the Defocus PD can be explained by the fact that in the performed simulations the first three images are equal. The author expects the method to exceed the results of Defocus PD even more, when the PD is optimized for multiple images ($N + 2^{th}$, $N + 3^{th}$). This is recommended for future research.

At lower Signal to Noise Ratios using the optimized PSNR is outperformed by using no PD at all and using Defocus PD. This could be because the Poisson noise is the main distortion in the image and it is image dependent, if the image is deteriorated extra by the PD this also influences this present noise. The fact that when the SNR is lower, the 8th Zernike polynomial (coma) often is used as part of the optimized PD, might also have influence on these results. Future research can be done on this.

Appendix A

Zernike Polynomials at Nolls order

Index	Noll's ordering	Name	Expression	Shape	PSF
$Z_0^0(x, y)$	1	piston	1		
$Z_1^1(x, y)$	2	tip	x		
$Z_1^{-1}(x, y)$	3	tilt	y		
$Z_2^0(x, y)$	4	defocus	$2x^2 + 2y^2 - 1$		
$Z_2^2(x, y)$	5	astigmatism	$x^2 - y^2$		
$Z_2^{-2}(x, y)$	6	astigmatism	$2xy$		
$Z_3^1(x, y)$	7	coma	$3x^3 + 3y^2x - 2x$		
$Z_3^{-1}(x, y)$	8	coma	$3y^3 + 3x^2y - 2y$		
$Z_3^3(x, y)$	9	trefoil	$x^3 - 3xy^2$		
$Z_3^{-3}(x, y)$	10	trefoil	$3x^2y - y^3$		
$Z_4^0(x, y)$	11	spherical	$6x^4 + 12y^2x^2 - 6x^2 + 6y^4 - 6y^2 + 1$		
$Z_4^2(x, y)$	12		$4x^4 - 3x^2 - 4y^4 + 3y^2$		
$Z_4^{-2}(x, y)$	13		$8yx^3 + 8y^3x - 6yx$		
$Z_4^4(x, y)$	14		$x^4 - 6y^2x^2 + y^4$		
$Z_4^{-4}(x, y)$	15		$4x^3y - 4xy^3$		

Figure A-1: The Zernike polynomials at Nolls order. On the right the Point Spread Functions of the different polynomials are given. Retrieved from [15].

Bibliography

- [1] D. Wilding, O. Soloviev, P. Pozzi, G. Vdovin, and M. Verhaegen, “Blind multi-frame deconvolution by tangential iterative projections (tip),” *Optics Express*, vol. 25, no. 26, pp. 32305–32322, 2017.
- [2] R. A. Gonsalves, “Phase retrieval and diversity in adaptive optics,” *Optical Engineering*, vol. 21, no. 5, p. 215829, 1982.
- [3] D. Wilding, P. Pozzi, O. Soloviev, G. Vdovin, and M. Verhaegen, “Pupil mask diversity for image correction in microscopy,” *Optics express*, vol. 26, no. 12, pp. 14832–14841, 2018.
- [4] D. Wilding, P. Pozzi, O. Soloviev, G. Vdovin, and M. Verhaegen, “Phase diversity based object estimation in light-sheet fluorescence microscopy,” in *Bio-Optics: Design and Application*, pp. BoTu2A–2, Optical Society of America, 2017.
- [5] T. G. Stockham, T. M. Cannon, and R. B. Ingebretsen, “Blind deconvolution through digital signal processing,” *Proceedings of the IEEE*, vol. 63, no. 4, pp. 678–692, 1975.
- [6] R. Paxman, “Diversity imaging,” in *Signal Recovery and Synthesis*, p. SWA1, Optical Society of America, 2001.
- [7] R. G. Paxman, T. J. Schulz, and J. R. Fienup, “Joint estimation of object and aberrations by using phase diversity,” *JOSA A*, vol. 9, no. 7, pp. 1072–1085, 1992.
- [8] R. A. Gonsalves and R. Chidlaw, “Wavefront sensing by phase retrieval,” in *Applications of Digital Image Processing III*, vol. 207, pp. 32–39, International Society for Optics and Photonics, 1979.
- [9] B. H. Dean and C. W. Bowers, “Diversity selection for phase-diverse phase retrieval,” *JOSA A*, vol. 20, no. 8, pp. 1490–1504, 2003.
- [10] M. W. Smith, “Use of adaptive optics to implement non quadratic phase diversity imaging,” in *Novel Optical Systems Design and Optimization VII*, vol. 5524, pp. 66–77, International Society for Optics and Photonics, 2004.

- [11] J. W. Jewett and R. A. Serway, *Physics for scientists and engineers with modern physics*. Cengage Learning EMEA, 2008.
- [12] R. J. Noll, “Zernike polynomials and atmospheric turbulence*,” *J. Opt. Soc. Am.*, vol. 66, pp. 207–211, Mar 1976.
- [13] R. Lane, A. Glindemann, and J. Dainty, “Simulation of a kolmogorov phase screen,” *Waves in random media*, vol. 2, pp. 209–224, 1992.
- [14] J. C. Wyant and K. Creath, “Basic wavefront aberration theory for optical metrology,” *Applied optics and optical engineering*, vol. 11, no. part 2, pp. 28–39, 1992.
- [15] M. Verhaegen, P. Pozzi, O. Soloviev, G. Vdovin, and D. Wilding, “Control for high resolution imaging, lecture notes for the course sc42030,” April 2017.
- [16] R. Szeliski, *Computer vision: algorithms and applications*. Springer Science & Business Media, 2010.
- [17] K. Pakhira Malay, *Digital image processing and pattern recognition*. PHI Learning Private Limited, 2011.
- [18] G. M. P. Van Kempen, *Image restoration in fluorescence microscopy*. Delft University Press, 1999.
- [19] J. Chung, S. Knepper, and J. G. Nagy, “Large-scale inverse problems in imaging,” *Handbook of Mathematical Methods in Imaging*, pp. 1–40, 2014.
- [20] P. C. Hansen, J. G. Nagy, and D. P. O’leary, *Deblurring images: matrices, spectra, and filtering*, vol. 3. Siam, 2006.
- [21] R. A. Gonsalves and R. H. Chidlaw, “Analytical studies of phase estimation techniques,” tech. rep., EIKONIX CORP BEDFORD MA, 1980.
- [22] D. Wilding, O. Soloviev, P. Pozzi, C. Smith, G. Vdovin, and M. Verhaegen, “Blind single-frame deconvolution by tangential iterative projections (tip),” *arXiv preprint arXiv:1810.07558*, 2018.
- [23] T. Samajdar and M. I. Quraishi, “Analysis and evaluation of image quality metrics,” in *Information Systems Design and Intelligent Applications* (J. K. Mandal, S. C. Satapathy, M. Kumar Sanyal, P. P. Sarkar, and A. Mukhopadhyay, eds.), (New Delhi), pp. 369–378, Springer India, 2015.
- [24] Z. Wang, A. C. Bovik, H. R. Sheikh, and E. P. Simoncelli, “Image quality assessment: from error visibility to structural similarity,” *IEEE transactions on image processing*, vol. 13, no. 4, pp. 600–612, 2004.
- [25] J. Tian, L. Chen, L. Ma, and W. Yu, “Multi-focus image fusion using a bilateral gradient-based sharpness criterion,” *Optics communications*, vol. 284, no. 1, pp. 80–87, 2011.
- [26] M. K. Sharma, C. Gaur, P. Senthilkumaran, and K. Khare, “Phase imaging using spiral-phase diversity,” *Applied Optics*, vol. 54, no. 13, pp. 3979–3985, 2015.

- [27] N. Miyamura, “Generalized phase diversity method for self-compensation of wavefront aberration using spatial light modulator,” *Optical Engineering*, vol. 48, no. 12, p. 128201, 2009.
- [28] Y. Shechtman, S. J. Sahl, A. S. Backer, and W. Moerner, “Optimal point spread function design for 3d imaging,” *Physical review letters*, vol. 113, no. 13, p. 133902, 2014.
- [29] E. R. Dowski and W. T. Cathey, “Extended depth of field through wave-front coding,” *Applied optics*, vol. 34, no. 11, pp. 1859–1866, 1995.
- [30] Q. Yang, L. Liu, and J. Sun, “Optimized phase pupil masks for extended depth of field,” *Optics Communications*, vol. 272, no. 1, pp. 56–66, 2007.
- [31] A. Yang, A. Yang, Q. Wang, and Z. Liu, “A novel blind deconvolution method for adaptive optics images based on wavelength diversity,” in *Tenth International Conference on Graphics and Image Processing (ICGIP 2018)*, vol. 11069, p. 1106935, International Society for Optics and Photonics, 2019.

Glossary

List of Acronyms

BMFD	Blind Multi-frame Deconvolution
CCD	Charge Coupled Device
CoM	Center of Mass
DCSC	Delft Center for Systems and Control
MSE	Mean Squared Error
MTF	Modulation Transfer Function
OTF	Optical Transfer Function
PD	Phase Diversity
PSF	Point Spread Function
PSNR	Peak Signal to Noise Ratio
RMS	Root Mean Square
SNR	Signal to Noise Ratio
SSIM	Structural Similarity
TIP	Tangential Iterative Projection
TU Delft	Delft University of Technology

